Spatially Heterogeneous Biofilm Simulations using an Immersed Boundary Method with Lagrangian Nodes Defined by Bacterial Locations

Jason F. Hammond[a], Elizabeth J. Stewart[d], John G. Younger[c], Michael J. Solomon[d], David M. Bortz[b,1,*]

[a]*AFRL, High Power Microwave Division*
[b]*Department of Applied Mathematics, University of Colorado Boulder*
[c]*Department of Emergency Medicine, University of Michigan Ann Arbor*
[d]*Department of Chemical Engineering, University of Michigan Ann Arbor*

Abstract

In this work we consider how surface-adherent bacterial biofilm communities respond in flowing systems. We simulate the fluid-structure interaction and separation process using the immersed boundary method. In these simulations we model and simulate different density and viscosity values of the biofilm than that of the surrounding fluid. The simulation also includes breakable springs connecting the bacteria in the biofilm. This allows the inclusion of erosion and detachment into the simulation. We use the incompressible Navier-Stokes (N-S) equations to describe the motion of the flowing fluid. We discretize the fluid equations using finite differences and use a geometric multigrid method to solve the resulting equations at each time step. The use of multigrid is necessary because of the dramatically different densities and viscosities between the biofilm and the surrounding fluid. We investigate and simulate the model in both two and three dimensions.

Our method differs from previous attempts of using IBM for modeling biofilm/flow interactions in the following ways: the density and viscosity of the biofilm can differ from the surrounding fluid, and the Lagrangian node locations correspond to experimentally measured bacterial cell locations from 3D images taken of *Staphylococcus epidermidis* in a biofilm.

Keywords: Navier-Stokes equation, biofilm, immersed boundary method, computational fluid dynamics, multigrid, viscoelastic fluid

1. Introduction

In this paper we investigate the response and fragmentation of a biofilm attached to the interior of a tube and subjected to a flowing fluid. Specifically, we study the mechanisms of biofilm fluid response and

---

*Corresponding author

Email addresses: `jason.hammond@kirtland.af.mil` (Jason F. Hammond), `ejstewar@umich.edu` (Elizabeth J. Stewart), `jyounger@med.umich.edu` (John G. Younger), `mjsolo@umich.edu` (Michael J. Solomon), `dmbortz@colorado.edu` (David M. Bortz)

URL: `http://mathbio.colorado.edu` (David M. Bortz)

[1]Math Biology Group, Applied Mathematics, 526 UCB, University of Colorado, Boulder, CO 80309-0526, Phone: (303) 492-7569, Fax: (303) 492-4066

detachment in terms of varying biofilm density, elasticity, and viscosity. In the simulations, we model biofilms attached to the walls of 3-dimensional square tubes using an extension of the immersed boundary method (IBM) (originally developed by Peskin [29]). Our approach differs from the traditional IBM in several ways. We use experimentally measured biofilm bacterial cell locations as initial positions for our Lagrangian nodes whereas traditional IBM refines the Lagrangian mesh along with the Eulerian mesh. As a result we also have to adapt the Dirac delta approximation to scale with the radius of the bacteria rather than with the mesh width.

In this introduction, we first provide a brief background on the biology and biomechanics of bacterial biofilms in 1.1. In Section 1.2, we discuss some alternative mathematical models that have been used to model biofilms (along with advantages and disadvantages). In Section 1.3, we introduce the immersed boundary method, and in 1.4, we discuss the significance of including variable viscosity.

1.1. Bacterial Biofilms

Biofilms are a phenotype of bacteria that are found in health, industrial and natural settings. In the medical field, biofilms occur on devices such as contact lenses, catheters, and mechanical heart valves. In industrial settings, they occur in and on water pipes, storage tanks, ship hulls, filters, food preparation facilities, etc. In natural settings, they can be found as slime on rocks in bodies of water or as dental plaque on teeth.

Physically, biofilms are immobile and consist of a community of bacterial cells embedded in a dense surface-adherent extracellular matrix (ECM) of polysaccharides. Biofilms are mechanically strong structures that tend to deform and fragment rather than completely dislodge when subjected to flows. Figure 1 on page 3 contains an electron micrograph of a biofilm of *Klebsiella pneumoniae*, clearly showing the ECM interconnecting the bacterial cells. The physical properties of the ECM are central to the growth, attachment, and detachment of biofilms. The focus of this work is on the biomechanical response of the ECM to fluid flow resulting in deformation and separation.

An important feature of biofilms is that they are known to behave like *viscoelastic fluids* [17]. In other words, they exhibit both viscous and elastic responses upon deformation. Describing the exact viscoelastic behavior has been the subject of much experimental, theoretical, and computational research [17, 38, 3, 28, 20, 19, 31, 33, 34, 32]. For example, Klapper et al. and Pavlosky et al. use a linear Jeffrey's constitutive law [17, 28] while Lau et al. use a Voigt standard linear solid model for viscoelastic materials [20]. Our model includes elasticity of the biofilm by using simple linear springs (as done in [2]) to connect the bacterial cells, and includes the viscosity of the biofilm with a modification of the constitutive equations for stress.

1.2. Mathematical Models of Biofilms

Much research into the mathematical modeling of biofilm growth and fluid/structure interactions has been conducted in the last three decades [33, 34, 32, 46, 47, 18, 19]. Below, we summarize several modeling
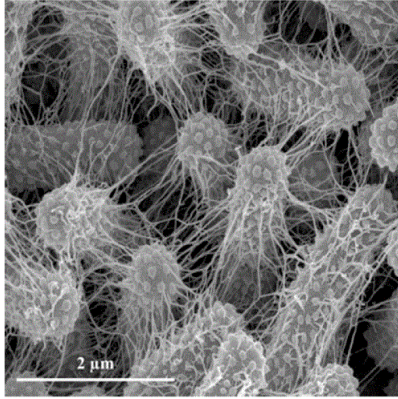
Figure 1: Scanning electron microscopy of sessile K. pneumoniae LM21 performed in mature biofilm formed on Thermanox slides in microfermentor system after 48 hours of development at 20000 times magnification. This image is from Balestrino et al. [5] (used with permission).

and simulation strategies. This is not intended to be exhaustive and we direct the interested reader to [44, 16] for more in-depth reviews.

The first attempts at mathematical modeling of biofilms were conducted in the early 1980s [36, 35, 15]. Picioreanu and others [19, 31, 18] advocated for an individual based (IB) approach, which models the behavior of each bacteria, encompassing ideas such as cell division, cell motility, metabolism, and death to simulate the growth and formation of colonies. Hybrid discrete-continuum models were the first methods to couple the flow with the the biofilm computationally in 2D and 3D simulations. Picioreanu, van Loodsdrecht, and Heijnen developed and used these hybrid discrete-continuum models to incorporate the flow over the irregular biofilm's surfaces, convective and diffusive mass transfer of substrate, bacterial growth, and biomass spreading [33, 34, 32].

The most sophisticated (purely) continuum models developed are the phase-field models, which use a one-fluid/two-component formulation in which the ECM and the bacteria are modeled as one fluid component, while the collective ensemble of nutrient substrates and the surrounding fluid are the other [46, 47]. Two-dimensional simulations of both biofilm growth and biofilm-flow interaction are presented in [47], in which shear induced deformation and detachment are illustrated.

We note that our model differs from both these approaches in the way that we model the biofilm. We treat the bacteria in the biofilm as discrete points, where the nodal locations in our simulations correspond to the locations of the bacterial cells within the biofilm. This contrasts from the continuum phase-field models that only include averaged biomechanical properties of the biofilm. With our mathematical formulation, just as in the individual based models, we can obtain the cumulative local stresses as well as attribute different local properties to the biofilm. Our model can be thought of as an extension of the individual based models, where we accurately account for the interactions with the fluid as well as include the possibility of fragmentation. We also assume that on the time scale of our simulations there is no biofilm growth; so we ignore such

factors as nutrient concentrations and growth rates.

1.3. Immersed Boundary Method

The overall goal is to simulate the response of a biofilm attached to the walls of both 2- and 3-dimensional square tubes. We do this using an extension of the immersed boundary method. In this section, we introduce the immersed boundary method and provide the framework necessary for us to later extend the IBM for our use.

The immersed boundary method (IBM) was originally developed by Peskin to study blood flow in the heart [29]. The IBM has been used previously to model and simulate biofilm/fluid interactions by Dillon, Fauci, et al. in [12], and by Alpkvist and Klapper in [2]. The authors successfully coupled the fluid to the biofilm; however, they make the assumption that the biofilm has the same density and viscosity as the surrounding fluid. This choice substantially simplifies the task of solving the N-S equations but does not account for the fact that biofilms typically have $500\times$ larger viscosity and 12% larger density than water [17, 37]. They also use a random distribution of points within a biofilm-shaped shell to represent the biofilm, which does not account for the true spatial distribution of bacterial cells within a biofilm.

The IBM has been used more recently in the modeling of immersed elastic structures in viscous flows in [14, 23, 49, 42], in which the authors use constitutive viscoelastic models including Maxwell, Voigt, and Jeffrey's models to incorporate forces in the immersed structures into the IBM. Similarly, our ultimate goal is to establish an appropriate constitutive model for the forces in the biofilm with the help of experimental collaborators and to include this in our IBM formulation.

1.4. Variable Viscosity

It is agreed upon in the biofilm research community that biofilms behave like a viscoelastic fluid. There has been a few efforts to match the behavior of biofilms with conventional mechanical viscoelastic models [17, 3, 28, 20]. However, these efforts have not produced a consensus on the model to use for viscoelasticity in biofilms. This is, in part, due to the fact that the viscoelastic properties in biofilms is highly variable with different growth conditions [10] and even in the same growth conditions [1].

The incorporation of spatially variable viscosity in the immersed boundary method is an area that has yet to be well developed. Luo et al. couple the immersed viscoelastic structure to the fluid flow in an immersed boundary type formulation, but they solve the fluid equations separately from the equations governing the motion of the immersed viscoelastic solid and then couple the solutions at their physical interface [23]. This formulation will not work in our case because we couple the biofilm to the fluid in the entire domain so that it will behave as a viscoelastic fluid. Another approach to including viscosity into the immersed boundary method is by replacing the simple elastic springs with viscoelastic links, which will change the value of the external force, $\mathbf{f}$, in the Navier-Stokes equations (Equation (26) below). This type of strategy was used first

by Bottino in [6] to model general viscoelastic connections in actin cytoskeleton of ameboid cells and also by Dillon and Zhuo in [49] to model sperm motility.

There are two natural ways to add viscosity to the biofilm. The first is through the use of local damping forces in addition to the springs that we use for the elastic component. In this way, we can define the forces between any two connected bacterial cells using a typical mechanical model for a viscoelastic material. The second way is to treat the entire domain as a continuous Newtonian viscous fluid with a spatially varying viscous coefficient. The use of dashpot damping with our current mathematical formulation is quicker to implement but has serious stability restrictions in the simulation, and thus we omit this method here.[2]

The approach in this work is to treat the fluid in the entire domain as a Newtonian viscous fluid with a spatially varying viscous coefficient. The core idea involves replacing the viscous term in the Navier-Stokes equation with one that can apply to nonuniform viscosity in the fluid. We note that to the best of our knowledge this approach has not yet been attempted in the single fluid immersed boundary method. There have been attempts using two materials (fluid-fluid or fluid-solid), coupling them at their interface, in which the stress is adapted in the viscoelastic fluid or solid to account for a different viscosity [47, 23]. However, in our approach, we couple the biofilm to the fluid within the entire biofilm region, not just at the interface. Thus, we must adapt the forces in the Navier-Stokes equations to account for the viscous and elastic stresses on the surface and within the biofilm.

We now describe the organization of this paper. In Section 2 we provide our mathematical formulation, which is a variation of the immersed boundary method literature. In Section 3, we describe our numerical method, based on a multigrid approach. In Section 4, we provide numerical validation of our method. In Section 5, we provide simulation results in both two and three dimensions, running our simulations for a variety of experimentally obtained biofilms with varying parameters such as spring constants, densities, viscosities. Finally, we provide conclusions in Section 7 and a discussion of possibilities for future work in Section 8.

2. Mathematical Formulation

In this section, we provide the mathematical formulation for our simulations. We use an Eulerian mesh to describe the system as a whole and solve the dimensionless N-S equations at each time step on this mesh. The Lagrangian nodes are used only to compute information about the biofilm (location, velocity, local density, force) and then transfer the information back onto the Eulerian mesh using the Dirac delta function.[3] For convenience, we provide a list in Appendix A of the variables and parameters used in this work.

---

[2]We will pursue this approach in future work when change our numerical scheme to a semi-implicit or implicit method.
[3]The Dirac Delta function is approximated in the actual implementation (see Equation (14)).

We now introduce the mathematical equations used in our model. The dependent Eulerian variables are velocity $\mathbf{u}(\mathbf{x}, t)$, pressure $p(\mathbf{x}, t)$, density $\rho(\mathbf{x}, t)$, and Eulerian force density $\mathbf{f}(\mathbf{x}, t)$, where $\mathbf{x}$ is the independent Eulerian variable and t is time. The dependent Lagrangian variables are position of the nodes $\mathbf{X}(\mathbf{q}, t)$, velocity of the nodes $\mathbf{U}(\mathbf{q}, t)$, and the Lagrangian force density $\mathbf{F}(\mathbf{q}, t)$, where $\mathbf{q} = (q, r, s)$ is the independent Lagrangian variable. The equations of motion for the biofilm-fluid interaction are

$$\rho(\mathbf{x}, t)\left(\frac{\partial \mathbf{u}}{\partial t} + \mathbf{u} \cdot \nabla \mathbf{u}\right) = -\nabla p + \nabla \cdot \left(\mu(\mathbf{x}, t)\left(\nabla \mathbf{u} + (\nabla \mathbf{u})^T\right)\right) + \mathbf{f}(\mathbf{x}, t) \tag{1}$$

$$\nabla \cdot \mathbf{u} = 0, \tag{2}$$

$$\frac{\partial \mathbf{X}}{\partial t}(\mathbf{q}, t) = \mathbf{U}(\mathbf{X}(\mathbf{q}, t), t), \tag{3}$$

$$\mathbf{f}(\mathbf{x}, t) = \int_{\Omega_b} \mathbf{F}(\mathbf{q}, t)\delta(\mathbf{x} - \mathbf{X}(\mathbf{q}, t))\mathrm{d}\mathbf{q}, \tag{4}$$

$$\rho(\mathbf{x}, t) = \rho_0 + \int_{\Omega_b} \rho_b \delta(\mathbf{x} - \mathbf{X}(\mathbf{q}, t))\mathrm{d}\mathbf{q}, \tag{5}$$

$$\mathbf{U}(\mathbf{X}(\mathbf{q}, t), t) = \int_{\Omega} \mathbf{u}(\mathbf{x}, t)\delta(\mathbf{x} - \mathbf{X}(\mathbf{q}, t))\mathrm{d}\mathbf{x}, \tag{6}$$

where μ is the dynamic viscosity, ρ_0 is the mass density of the fluid, ρ_b is the additional mass density of the biofilm from that of the surrounding fluid, Ω is the flow domain, $\Omega_b \subset \Omega$ is the space occupied by only the biofilm, and $\delta(\mathbf{x})$ is the Dirac delta function. Equations (1) and (2) are the incompressible Navier-Stokes (N-S) equations with spatially varying viscosity and a forcing term that represents the forces applied by the biofilm on the fluid. Equation (3) is the equation of motion of the biofilm, where $\mathbf{U}(\mathbf{q}, t)$ is the velocity of the biofilm. The systems of PDE's given by (1)-(2) is coupled to (3) by the integrals given in (4)-(6).

To avoid numerical inaccuracies due to roundoff errors, we non-dimensionalize these equations using the non-dimensional variables defined as

$t^* = \frac{t}{T}, \qquad \mathbf{x}^* = \frac{\mathbf{x}}{L}, \qquad \mathbf{u}^* = \frac{\mathbf{u}}{u_0}, \qquad p^* = \frac{p - p_{L_{tube}}}{p_0 - p_{L_{tube}}},$

$\nabla^* = L\nabla, \qquad \rho^* = \frac{\rho}{\rho_0}, \qquad \mathbf{f}^* = \frac{\mathbf{f}}{f_0}, \qquad \mu^* = \frac{\mu}{\mu_0},$

where p_0 is the pressure at the upstream end of the tube, $p_{L_{tube}}$ is the pressure at the downstream end of the tube, T is the characteristic time scale, f_0 is the characteristic force density, and L is the characteristic length. We use the scaling parameters defined in Table B.10 on page 43. Dropping the stars from the dimensionless variables, equations (2) and (4)-(6) remain the same as in the case with dimensions, while equations (1) and (3) become

$$\sigma\rho(\mathbf{x}, t)\frac{\partial \mathbf{u}}{\partial t} + \rho(\mathbf{x}, t)\mathbf{u} \cdot \nabla \mathbf{u} = -\varepsilon\nabla p + Re^{-1}\nabla \cdot \left(\mu(\mathbf{x}, t)\left(\nabla \mathbf{u} + (\nabla \mathbf{u})^T\right)\right) + \frac{Lf_0}{\rho_0 u_0^2}\mathbf{f}(\mathbf{x}, t), \tag{7}$$

$$\sigma\frac{\partial \mathbf{X}}{\partial t}(\mathbf{q}, t) = \mathbf{U}(\mathbf{q}, t), \tag{8}$$

where $\sigma = \frac{L}{Tu_0}$ is the Strouhal number, $\varepsilon = \frac{p_0 - p_{L_{tube}}}{\rho_0 u_0^2}$ is the Euler number, and $Re = \frac{\rho_0 L u_0}{\mu}$ is the Reynolds number of the fluid.

The initial velocity profile is the exact solution to the incompressible Navier-Stokes equations in a square or circular tube with rigid walls and no-slip conditions at the walls. The velocity profile for a circular cylinder

can be found in many textbooks in fluid dynamics (such as [45]), and a series solution for the laminar flow velocity profile for a square tube was derived by Spiga and Morini in [40].

3. Numerical Method

In this section, we describe the numerical formulation for our simulations. Our numerical task is to solve the system defined by Equations (1)-(6), and we now provide the details of our numerical approach.

The incompressible flow Navier-Stokes equations, (1)-(2), are discretized on a fixed uniform Eulerian lattice, while the biofilm equations are discretized on a moving Lagrangian array of points that do not necessarily coincide with the fixed Eulerian mesh points of the fluid computation. We represent the interaction equations (4)-(6) with a smoothed approximation $\tilde{\delta}$ to the Dirac delta function (see 3.1). Our numerical approach was inspired by the solving technique used by Zhu and Peskin in [48] to simulate a flapping filament in a soap film.

The discretized equations corresponding to (4)-(6) are given by

$$\mathbf{f}^n(\mathbf{x}) \quad = \quad \sum_{s=1}^{\eta} \mathbf{F}^n(s)\tilde{\delta}(\mathbf{x} - \mathbf{X}^n(s), \, \omega), \tag{9}$$

$$\rho^n(\mathbf{x}) \quad = \quad \rho_0 + \sum_{s=1}^{\eta} \rho_b \tilde{\delta}(\mathbf{x} - \mathbf{X}^n(s), \, \omega)d_0^3, \tag{10}$$

$$\mathbf{U}^{n+1}(s) \quad = \quad \sum_{\mathbf{x}} \mathbf{u}^{n+1}(\mathbf{x})\tilde{\delta}(\mathbf{x} - \mathbf{X}^n(s), \, h)h^3, \tag{11}$$

where the superscript n denotes numerical approximations at a particular time step n, η is the total number of Lagrangian discretization points, the sum in (11) is over all the discrete points of the form $\mathbf{x} = (ih, \, jh, \, kh)$ with i, j, and k are integers, h is the Eulerian mesh width, and d_0^3 is the average volume element of the Lagrangian nodes (computed by dividing the total volume of the biofilm by the total number of Lagrangian nodes distributed within it). Following convention, we replace $(q, \, r, \, s)$ from the mathematical formulation with only s, which we use as an indexed label with a unique number assigned to each Lagrangian point [48]. In (9), $\mathbf{F}(s)$ is now the total elastic force on the Lagrangian node associated with marker s, as opposed to an elastic force density. This is because we calculate the force explicitly depending on which other nodes it is connected to.

3.1. Dirac Delta Approximation

In [30], Peskin defines $\delta_h(\mathbf{x})$ as

$$\delta_h(\mathbf{x}) = h^{-3}\phi\left(\frac{x}{h}\right)\phi\left(\frac{y}{h}\right)\phi\left(\frac{z}{h}\right) \qquad , \tag{12}$$

where $\phi(r)$ is

$$\phi(r) = \phi_1 = \begin{cases} \frac{1}{8}\left(3 - 2|r| + \sqrt{1 + 4|r| - 4r^2}\right); & \text{if } |r| \leq 1, \\ \frac{1}{8}\left(5 - 2|r| - \sqrt{-7 + 12|r| - 4r^2}\right); & \text{if } 1 \leq |r| \leq 2, . \\ 0; & \text{if } |r| \geq 2. \end{cases} \tag{13}$$

7

We replace this δ_h, that is used in standard IBM implementations, with one that scales with ω instead of h as

$$\tilde{\delta}(\mathbf{x}, \omega) = \omega^{-3} \phi\left(\frac{x}{\omega}\right) \phi\left(\frac{y}{\omega}\right) \phi\left(\frac{z}{\omega}\right). \tag{14}$$

We deviate from the standard scaling of the Dirac Delta approximation for two reasons. The first is that we wish to give a presence to the bacterial cells that is representative of the true volume of the cells. Thus, in the simulations, we make ω in (9) and (10) equal to the radius of a bacterial cell that we are modelling. Equation (9) then spreads the force over a volume that is slightly larger than the cell, ensuring that the entire space occupied by the cell in the fluid is influenced by the force. The second reason we use this scaling is because, during the mesh refinement analysis described in 4.3.3, we discovered that the implementation with the scaling by h restricts us to less than first-order convergence of the velocity, $\mathbf{u}$. Using a scaling that is independent of the mesh-width fixes this issue and leads to greater than first order convergence.

However, this modification does have the negative consequence of losing two desirable conditions that were previously satisfied by the Dirac delta approximation, δ_h. Specifically, with δ_h as defined in (13), the *unity condition,*

$$\sum_{\mathbf{x} \in g_h} \delta_h(\mathbf{x} - \mathbf{X})h^3 = 1, \ \forall \mathbf{X}, \tag{15}$$

and the *first-moment condition,*

$$\sum_{\mathbf{x} \in g_h} (\mathbf{x} - \mathbf{X})\delta_h(\mathbf{x} - \mathbf{X})h^3 = 0, \ \forall \mathbf{X}, \tag{16}$$

are both satisfied. However, using $\tilde{\delta}$ in place of δ_h, these conditions fail to hold true for all $\mathbf{X}$ when $\omega \neq h$. In practice, this is not a major concern as many IBM formulations use a Dirac delta approximation that satisfies the unity condition, (15), but does not satisfy the first-moment condition, (16). For example, in [48], Peskin and Zhu replace $\phi(r)$ in δ_h with

$$\phi(r) = \phi_2 = \begin{cases} \frac{1}{4}\left(1 + \cos\left(\frac{\pi r}{2}\right)\right); & \text{if } |r| \leq 2, \\ 0; & \text{if } |r| > 2. \end{cases} \tag{17}$$

We do have to choose whether we want to use $\phi(r)$ as defined by (13) or by (17). For either choice of ϕ, it is true that both

$$\lim_{h \to 0} \int \tilde{\delta}(\mathbf{x} - \mathbf{X})d\mathbf{x} = 1$$

and

$$\lim_{h \to 0} \int (\mathbf{x} - \mathbf{X})\tilde{\delta}(\mathbf{x} - \mathbf{X})d\mathbf{x} = 0.$$

Note that, in the limit as $h \to 0$, we see greater than $O(h^2)$ convergence to (15) and (16) (see Figure 2 on page 10), which is consistent with the theoretical convergence rate for a Riemann sum. Therefore, we choose to use the ϕ for which the summations in (15) and (16) are closest to 1 and 0, respectively, for the values of

ω and h used in our simulations so that we can have the most accurate discrete approximation of the Dirac delta function.

We now define two error metrics to determine how well $\tilde{\delta}$ (using either ϕ_1 or ϕ_2) satisfies the unity and first-moment conditions. Analogous metrics and comparisons could be conducted in higher dimensions, but for simplicity we provide a one-dimensional comparison. Using $\omega = \frac{1}{100}$ and the one-dimensional version of (14), we define

$$\epsilon_{unity}(\omega, h) = \max_{\mathbf{X} \in [0,h]} \left| \left(\sum_{\mathbf{x} \in g_h} \tilde{\delta}(\mathbf{x} - \mathbf{X}, \omega)h \right) - 1 \right| \tag{18}$$

and

$$\epsilon_{mom}(\omega, h) = \max_{\mathbf{X} \in [0,h]} \left| \sum_{\mathbf{x} \in g_h} (\mathbf{x} - \mathbf{X}) \, \tilde{\delta}(\mathbf{x} - \mathbf{X}, \omega)h \right|. \tag{19}$$

We only have to find the maximum over $\mathbf{X} \in [0, h]$ since the summations are periodic with period h, because $\mathbf{X} = 0$ and $\mathbf{X} = h$ both correspond to a Lagrangian point being at the same location as an Eulerian point. We find $\epsilon_{unity}(1/100, h)$ and $\epsilon_{mom}(1/100, h)$ for values of $h \in \left(\frac{1}{1024}, \frac{1}{100} \right)$ and using both ϕ_1 and ϕ_2. These values are compared in Figure 2 on page 10, and show that using ϕ_2 provides a better approximation of the Dirac delta function in terms of matching the values of these summations for most values of h. Notice too, that the values of ϵ_{unity} and ϵ_{mom} are exactly zero for certain relationships between h and ω. For example, if $h = \frac{\omega}{z}$ with $z \in \mathbb{N}$, then ϵ_{unity} and ϵ_{mom} are exactly zero when using ϕ_1. Thus if our problem allows for $h = \frac{\omega}{z}$, then we would use ϕ_1. However, with the choices we have made for ω and h in our numerical scheme, it is a better choice to use ϕ_2 in our simulations.

In the transfer of information from the Lagrangian grid to the Eulerian grid, we scale ϕ by ω (see (9) and (10)). However, in the transfer of velocity from the Eulerian to Lagrangian grid (Eq. (11)), we scale ϕ with h instead of ω in order to capture the velocity only at the center of mass of the bacterial cells.

3.2. Elastic Forces

In [2], Alpkvist and Klapper use Hooke's Law to describe the elastic force between the connected Lagrangian nodes. We also use this method as our first attempt to model the interconnecting force in the biofilm. Thus, the elastic force on each Lagrangian point using Hooke's Law is

$$\mathbf{F}^n(s) = \sum_{k=1}^{\eta} I_{s,k} \frac{\mathbf{d}_{s,k}}{d_{s,k}} T_{s,k}, \tag{20}$$

where T is the tension between nodes s and k, I is the connectivity matrix defined as

$$I_{s,k} = \begin{cases} 1 & \text{bacteria } s \text{ connected to bacteria } k \\ 0 & \text{otherwise}, \end{cases}$$

and $\mathbf{d}_{s,k}$ is the vector pointing from Lagrangian node s to k with magnitude $d_{s,k}$. The tension from the spring connecting node s and k is formulated as
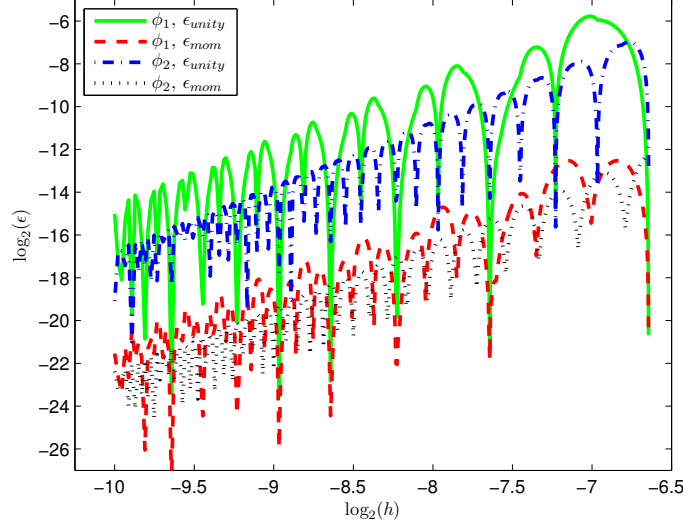
$$T_{s,k} = K_{s,k}(d_{s,k} - r_{s,k}),$$

9

Figure 2: We show $\epsilon_{unity}(1/100, h)$ and $\epsilon_{mom}(1/100, h)$ for $h \in \left(\frac{1}{1024}, \frac{1}{100}\right)$. ϕ_1 is the ϕ given in (13) and ϕ_2 is the ϕ given in (17). We show $\log_2$ in the x and y axes so that the convergence rate appears as the slope of the line segments.

where $r_{s,k}$ is the rest length of the spring connecting nodes s and k, and $K_{s,k}$ is its Hookean spring coefficient. We choose to define each spring coefficient as

$$K_{s,k} = \frac{F_{max}}{r_{s,k}}, \tag{21}$$

where F_{max} is the force required to break the spring. We define the spring coefficients in this way to ensure that all of the springs, regardless of initial length, break with a force of F_{max} when they are stretched to a length of $2r_{s,k}$. In our simulations, we vary F_{max} to attain specific results (such as detachment; see 5.1 more details). As is done in [2], we model the failure of the ECM by breaking the connections between the Lagrangian nodes as the springs used to connect them exceed twice their resting length. We note that this condition, however, is not based on experimental evidence, and in future work we will adapt this breaking criteria according to experimental results. In Section 8, we discuss future adaptations to the breaking criteria in terms of the yield stress of polymers.

We conclude this section with a 1D illustration to show how 3 linearly connected cells transfer their elastic forces to the Eulerian grid via Equation (9), and how this is effected by varying h (see Figure 3 on page 11). In this example, the three nodes are close enough to each other that their forces add in the overlapping regions. Sub-figures (b)-(e) illustrate how, with finer discretizations (smaller h), the elastic forces on the bacteria are more accurately represented in the Eulerian grid.
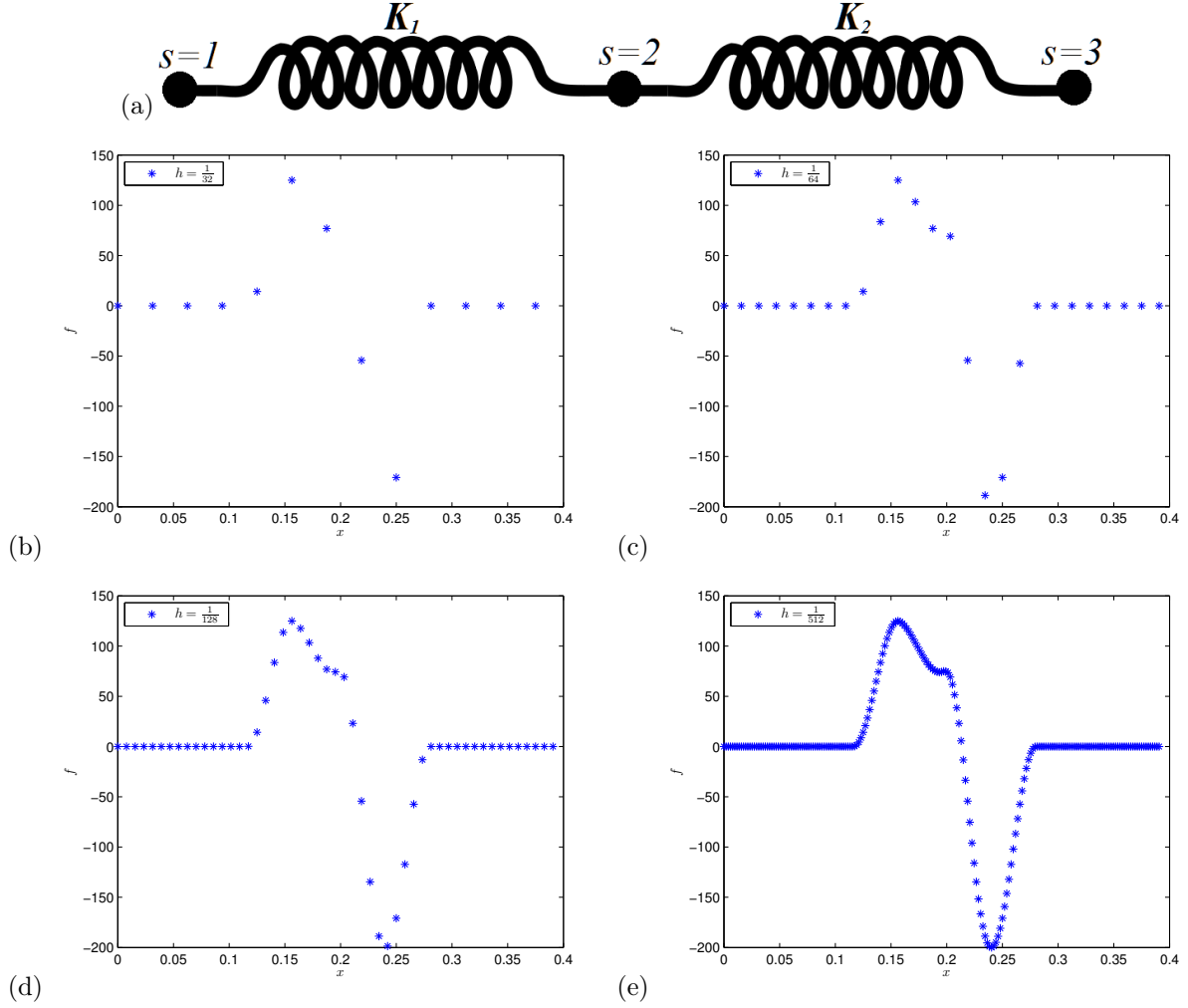
Figure 3: Examples of 1D $f(x)$ with three Lagrangian nodes (a), one at $X(s=1) = 5/32$ on an Eulerian node and the others at $X(s=2) = \frac{5}{32} + \frac{2\pi}{150}$ and $X(s=3) = \frac{5}{32} + \frac{4\pi}{150}$ (this position is chosen so that the second and third nodes are close enough to the first one to show the interaction of the forces), with $\omega = \frac{1}{50}$. These positions were chosen so that the cells would be close enough to each other to have an overlapping region on the Eulerian grid after the transfer of the forces from the Lagrangian grid. In this demonstration, $F(s=1) = 5$, $F(s=3) = -8$, and $F(s=2) = -(F(1) + F(3)) = 3$. These plots illustrate the effect of using different spatial steps: (b) $h = \frac{1}{32}$, (c) $h = \frac{1}{64}$, (d) $h = \frac{1}{128}$, (e) $h = \frac{1}{512}$.

11
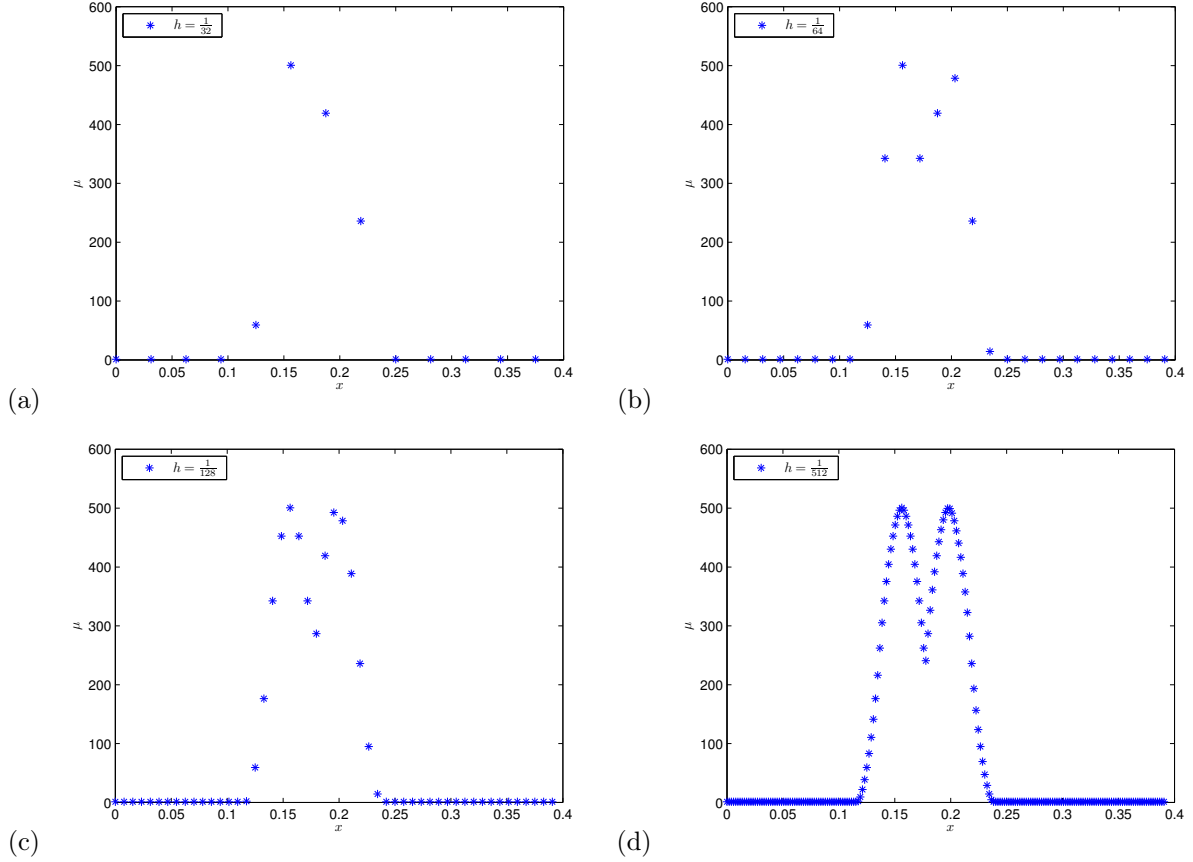
Figure 4: Examples of 1D $\mu(x)$ with two Lagrangian nodes, one at $x = 5/32$ on an Eulerian node and the other at $x = \frac{5}{32} + \frac{2\pi}{150}$, with $\omega = \frac{1}{50}$. These Lagrangian nodes (cells) are close enough that there is a region of interaction. These plots illustrate the effect of using different spatial steps: (a) $h = \frac{1}{32}$, (b) $h = \frac{1}{64}$ (c) $h = \frac{1}{128}$ (d) $h = \frac{1}{512}$

3.3. Variable Viscosity

It is known that ECM density decreases with distance from an individual cell. To account for this, the exact form of $\mu(\mathbf{x})$ used in our simulations is

$$\mu(\mathbf{x}) = \max_{1 \le s \le \eta, \, s \in \mathbb{N}} \left[(2\omega)^D \left(\mu_{max} - \mu_{out} \right) \tilde{\delta}(\mathbf{x} - \mathbf{X}(s), \, \omega) + \mu_{out} \right], \tag{22}$$

where μ_{max} is the viscosity at a bacterial node, μ_{out} is the viscosity of the surrounding fluid, D is the spatial dimension, and ω is a parameter we can use to stretch the influence of the additional viscosity. We made this choice for $\mu(\mathbf{x})$ because we wanted a viscosity that would decrease at the same rate as the elastic force with the distance from the bacterial cell. See Figure 4 on page 12 for a 1D example of the effect of ω and h on the viscosity distribution, $\mu(\mathbf{x})$, from two interacting cells. In the future, we can change this function to suit the specific viscous properties of the particular biofilm.

3.4. Solution Strategy

We employ a *projection method* ([8]) to solve the incompressible Navier-Stokes equations numerically, building on the method used by Zhu and Peskin in [48]. This method introduces a velocity field (at an intermediate time), $\tilde{\mathbf{u}}(\mathbf{x}, t)$, which is the solution to the difference equation

$$\rho^n \left(\sigma \frac{\tilde{\mathbf{u}}_k^{n+1} - \mathbf{u}_k^n}{\triangle t} + \frac{1}{2}(\mathbf{u} \cdot \mathbf{D}^0 \mathbf{u}_k + \mathbf{D}^0 \cdot (\mathbf{u}\mathbf{u}_k))^n \right) = \frac{1}{Re}\mathbf{D}^0 \cdot \left(\mu^n \left(\mathbf{D}^0 \tilde{\mathbf{u}}_k^{n+1} + D_{h,k}^0 \tilde{\mathbf{u}}^{n+1} \right) \right) + \frac{Lf_0}{\rho_0 u_0^2} \mathbf{f}_k^n, \quad (23)$$

where $k = 1, 2, 3$ and the subscripts k denote the kth component of that vector. The finite difference operators in (23) are originally defined by

$$L_h(\phi(\mathbf{x})) = \sum_{i=1}^3 \frac{\phi(\mathbf{x} + h\mathbf{e}_i) + \phi(\mathbf{x} - h\mathbf{e}_i) - 2\phi(\mathbf{x})}{h^2},$$

$$D_{h,i}^0(\phi) = \frac{\phi(\mathbf{x} + h\mathbf{e}_i) - \phi(\mathbf{x} - h\mathbf{e}_i)}{2h},$$
$$\mathbf{D}^0 = (D_{h,1}^0, D_{h,2}^0, D_{h,3}^0),$$

where $\mathbf{e}_i$ is the unit vector in the ith direction. Additionally, $\mathbf{D}^0 \cdot \left(a\mathbf{D}^0 \phi \right)$ is defined for scalar functions, $a(\mathbf{x})$ and $\phi(\mathbf{x})$, using the midpoint values of a as

$$\mathbf{D}^0 \cdot \left(a\mathbf{D}^0 \phi \right) = \sum_{i=1}^3 \frac{a\left(\mathbf{x} + \frac{h}{2}\mathbf{e}_i\right) \frac{\phi(\mathbf{x}+h\mathbf{e}_i)-\phi(\mathbf{x})}{h} - a\left(\mathbf{x} - \frac{h}{2}\mathbf{e}_i\right) \frac{\phi(\mathbf{x})-\phi(\mathbf{x}-h\mathbf{e}_i)}{h}}{h}, \quad (24)$$

and $\mathbf{D}^0 \cdot \left(aD_{h,k}^0 \mathbf{u} \right)$ is defined as

$$\begin{aligned}
\mathbf{D}^0 \cdot \left(aD_{h,k}^0 \mathbf{u} \right) &= \frac{a\left(\mathbf{x} + \frac{h}{2}\mathbf{e}_k\right) \frac{\mathbf{u}_k(\mathbf{x}+h\mathbf{e}_k)-\mathbf{u}_k(\mathbf{x})}{h} - a\left(\mathbf{x} - \frac{h}{2}\mathbf{e}_k\right) \frac{\mathbf{u}_k(\mathbf{x})-\mathbf{u}_k(\mathbf{x}-h\mathbf{e}_k)}{h}}{h} + \\
&+ \sum_{i \neq k}^3 \left(\frac{a\left(\mathbf{x} + h\mathbf{e}_i\right) \frac{\mathbf{u}_i(\mathbf{x}+h\mathbf{e}_i+h\mathbf{e}_k)-\mathbf{u}_i(\mathbf{x}+h\mathbf{e}_i-h\mathbf{e}_k)}{2h}}{2h} \right. \\
&\left. - \frac{a\left(\mathbf{x} - h\mathbf{e}_i\right) \frac{\mathbf{u}_i(\mathbf{x}-h\mathbf{e}_i+h\mathbf{e}_k)-\mathbf{u}_i(\mathbf{x}-h\mathbf{e}_i-h\mathbf{e}_k)}{2h}}{2h} \right).
\end{aligned} \quad (25)$$

Note that in the case of constant viscosity, using the incompressibility constraint, (1) is reduced to the standard N-S equation used in IBM,

$$\rho(\mathbf{x}, t) \left(\frac{\partial \mathbf{u}}{\partial t} + \mathbf{u} \cdot \nabla \mathbf{u} \right) = -\nabla p + \mu \triangle \mathbf{u} + \mathbf{f}(\mathbf{x}, t). \quad (26)$$

Therefore, in the case of constant viscosity, equation (23) is replaced with

$$\rho^n \left(\sigma \frac{\tilde{\mathbf{u}}_k^{n+1} - \mathbf{u}_k^n}{\triangle t} + \frac{1}{2}(\mathbf{u} \cdot \mathbf{D}^0 \mathbf{u}_k + \mathbf{D}^0 \cdot (\mathbf{u}\mathbf{u}_k))^n \right) = \frac{1}{Re}L_h(\tilde{\mathbf{u}}_k^{n+1}) + \frac{Lf_0}{\rho_0 u_0^2} \mathbf{f}_k^n. \quad (27)$$

We solve (27) as opposed to (23) in the constant viscosity case, since each component of $\tilde{\mathbf{u}}$, $\tilde{\mathbf{u}}_k$, is independent of each other in (27), and can therefore be solved for separately and simultaneously.

13

To complete the discretized incompressible Navier-Stokes system, we have the following two equations:

$$\sigma \rho^n \left(\frac{\mathbf{u}^{n+1} - \tilde{\mathbf{u}}^{n+1}}{\triangle t} \right) = -\varepsilon \mathbf{D}^0 p^{n+1}, \tag{28}$$

$$\mathbf{D}^0 \cdot \mathbf{u}^{n+1} = 0. \tag{29}$$

We point out here that summing equations (23) and (28) leads to the discretized version of (26), with the exception that the evaluation of the viscous term is at the intermediate value of the velocity. We solve for pressure by applying $\mathbf{D}^0$ to both sides of (28) and using (29) to obtain

$$\mathbf{D}^0 \cdot \left(\frac{1}{\rho^n} \mathbf{D}^0 p^{n+1} \right) = \frac{\sigma}{\varepsilon} \frac{\mathbf{D}^0 \cdot \tilde{\mathbf{u}}^{n+1}}{\Delta t}. \tag{30}$$

To solve equations (23) and (30), we use Gauss-Seidel as a smoother in a multigrid solver. At each time step, we solve (27) for $\tilde{\mathbf{u}}^{n+1}$, substitute it into (30), solve for p^{n+1}, and finally solve for u^{n+1} using (28). Then the velocity is transferred from the Eulerian points to the Lagrangian points using (11). With $\mathbf{U}^{n+1}$ computed, the new Lagrangian node locations are computed using Euler's method as

$$\mathbf{X}^{n+1}(s) = \frac{\Delta t}{\sigma} \mathbf{U}^{n+1}(s) + \mathbf{X}^n(s).$$

The forces between the Lagrangian points are then recalculated and transferred to the Eulerian points using (9). Finally, the values of ρ^n and μ^n are evaluated using the new Lagrangian locations.

3.5. Multigrid

In this section, we discuss the elements of multigrid that we use in our solution strategy. For more details on multigrid, see [7].

In our solver, we use the conventional Gauss-Seidel iterative method with red-black ordering. In the multigrid scheme, we use full-weighting restriction to go from fine to coarse grids, and we use linear interpolation to go from coarse back to fine grids. The finest grid is the grid with step size h and the grids become coarser by increasing the step size by a factor of 2. This halves the number of nodes in each dimension, allowing for significantly faster computations on the coarser grids. The number of levels in the multigrid solver depends on both the dimensions of the computational domain as well as h. In our simulations, we iterate using multigrid V-cycles until we reach a sufficiently low value for the norm of the residual,

$$\left\| f^h - A^h \tilde{v}^h \right\|,$$

at each time step. Here, $A^h v^h = f^h$ is the linear discretization of a PDE, and the residual is $r^h = f^h - A^h \tilde{v}^h$, where $\tilde{v}$ is an approximation to v. The residual provides a bound on the true error in the solution of the linear system since we have this relationship between the error and the relative residual error:

$$\frac{\left\| e^h \right\|}{\left\| v^h \right\|} \leq cond(A^h) \frac{\left\| r^h \right\|}{\left\| f^h \right\|}, \tag{31}$$

where $e^h = v^h - \tilde{v}^h$, $r^h = f^h - A^h \tilde{v}^h$, and $cond(A^h)$ is the condition number of A^h [4]. In Section 4, we give approximations for the condition numbers for our matrices.
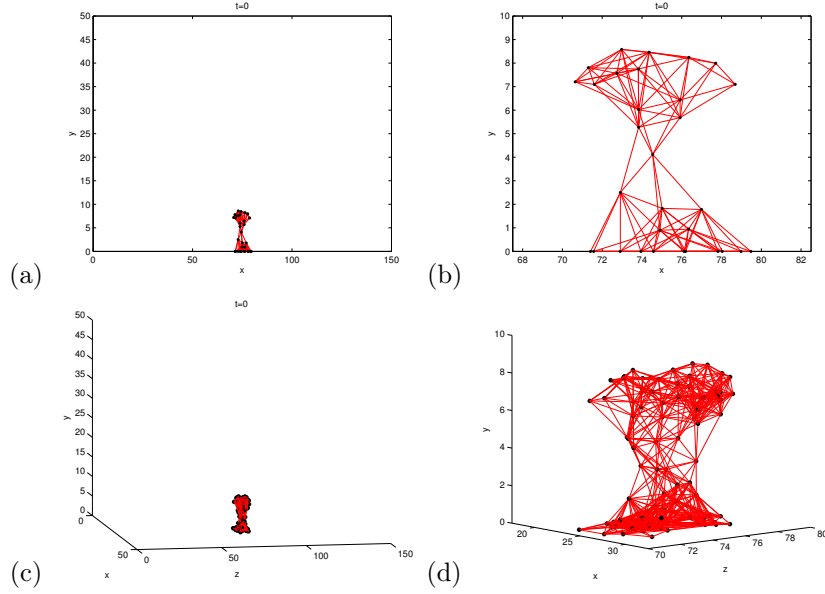
14

Figure 5: Shows examples of the computational domains with a sample biofilm. Axes units are microns. (a) is 2 dimensional and (c) is 3 dimensional. (b) and (d) show enlarged images of the biofilms. The points shown in these plots show the initial position of all of the bacterial cells in the biofilm.

3.6. Boundary Conditions

The computational domain used in our example simulations is a section of a tube with the biofilm centered in the direction along the axis of the tube (see Figure 5 on page 15). In the 2D case, flow is along the x-axis and, in 3D, it is along the z-axis. The boundary conditions we used in these simulations were derived from exact solutions for the velocity and pressure in the case of laminar flow. We now provide the boundary conditions in both the 2D and 3D cases.

3.6.1. 2D Boundaries

The no-slip boundary condition exists at the walls of tube and requires that the velocity be zero there, so we use that as the boundary condition at the walls. The velocity at the upstream boundary ($x = 0$) is held at the laminar flow velocity (shown in Figure 6 on page 17(a)) given by

$$u_1(y) = \frac{\kappa}{2\mu}(y^2 - 2ay), \tag{32}$$

where a is the radius of the tube, y is the displacement from the bottom edge of the tube, κ is the linear rate at which the pressure decreases through the tube, and u_1 is the x-component of the velocity (i.e., $\mathbf{u} = (u_1, u_2)$). At the downstream boundary, a Neumann condition is applied to the velocity by enforcing that

$$\left(\frac{\partial}{\partial x}\mathbf{u}(x,y)\right)_{x=x_{down}} = 0 \qquad \forall y,$$

where x_{down} represents the x value at the downstream boundary.

15

The boundary conditions for pressure come from the laminar flow equation for pressure given by

$$p(x) = \kappa x + p(0). \tag{33}$$

In our simulations, we hold the pressure at the upstream boundary at $p(0)$ and at $p(x_{down})$ at the downstream. At the top boundary, we hold the pressure at the values given by (33) and, at the bottom boundary (the boundary on which the biofilm is attached), we use a Neumann boundary

$$\left(\frac{\partial}{\partial y} p(x,y) \right)_{y=0} = 0, \qquad \forall x.$$

3.6.2. 3D Boundaries

In the 3D simulations, we orient the square tube along the z-axis (see Figure 5 on page 15(c)). The no-slip boundary condition exists at the walls of tube and requires that the velocity be zero there so we use that as the boundary condition at the walls. Derived by Spiga in [40], the velocity at the upstream boundary is held at the laminar flow velocity (shown in Figure 6 on page 17(b)) given by

$$u_3(x,y) = -\frac{16\kappa a^2}{\mu \pi^4} \sum_{n,m>0,\, \text{odd}} \frac{\sin\left(n\pi x/a\right)\sin\left(m\pi y/a\right)}{nm\left(n^2 + m^2\right)}, \tag{34}$$

where a is the width of the tube and u_3 is the z-component of the velocity (i.e., $\mathbf{u} = (u_1, u_2, u_3)$). At the downstream boundary, a Neumann condition is applied to the velocity by enforcing that

$$\left(\frac{\partial}{\partial z} \mathbf{u}(x,y,z) \right)_{z=z_{down}} = 0 \qquad \forall x,\, y.$$

The boundary conditions for pressure come from the laminar flow equation for pressure given by

$$p(z) = \kappa z + p(0), \tag{35}$$

where $z = 0$ is the upstream boundary. In our simulations, we hold the pressure at the upstream boundary at $p(0)$ and at $p(z_{down})$ at the downstream. At the top and side boundaries, we hold the pressure at the values given by Equation (35) and, at the bottom boundary (side with attached biofilm), we use the Neumann condition given by

$$\left(\frac{\partial}{\partial y} p(x,y,z) \right)_{y=0} = 0 \qquad \forall x,\, z.$$

4. Validation

It is crucial to validate our numerical method using known results and mesh refinement convergence analysis. Thus, below we provide numerical evidence that both our 2D and 3D simulations and numerical methods are working as they should.
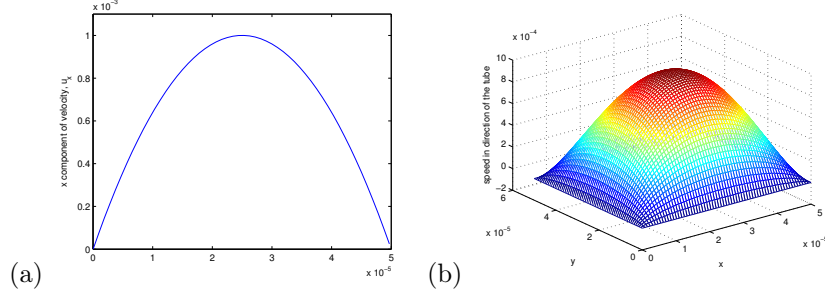
Figure 6: We illustrate upstream boundary conditions: (a) 2D laminar flow velocity profile, (b) 3D laminar flow velocity profile. Units are in meters for (a) and (b).

For the purposes of the 2D and 3D convergence analysis conducted in later sections, we require the following notation. We present the following notation in 3D (the 2D versions are analogous but without the z elements). Define the *Eulerian grid function p-norm* for an arbitrary 3D vector field, $\mathbf{w}(\mathbf{x}) = (w_1(\mathbf{x}), w_2(\mathbf{x}), w_3(\mathbf{x}))$, by

$$\|\mathbf{w}\|_p = \left(\sum_{i,j,k} |\mathbf{w}(x_i, y_j, z_k)|^p h^D \right)^{1/p}, \tag{36}$$

where D is the spatial dimension, $1 \le p < \infty$, and

$$|\mathbf{w}(x_i, y_j, z_k)| = \sqrt{w_1(x_i, y_j, z_k)^2 + w_2(x_i, y_j, z_k)^2 + w_3(x_i, y_j, z_k)^2}.$$

Then

$$\|\mathbf{w}\|_\infty = \max_{i,j,k} |\mathbf{w}(x_i, y_j, z_k)|.$$

Additionally, on the Lagrangian grid define the *Lagrangian grid function p-norm* for a vector field, $\mathbf{X} = (X_1(s), X_2(s), X_3(s))$, as

$$\|\mathbf{X}\|_p = \left(\sum_{s=1}^{\eta} |(X_1(s),\ X_2(s),\ X_3(s))|^p\, d_0^D \right)^{1/p},$$

where $1 \le p < \infty$ and d_0^D is the average volume element of the Lagrangian nodes. Then

$$\|\mathbf{X}\|_\infty = \max_{1 \le s \le \eta} |(X_1(s),\ X_2(s),\ X_3(s))|.$$

Note that both of these grid function norms are derived from using discretizations of the integrals used in a typical function p-norm (see Appendix A of [21] for more details).

There are three parts to our simulation validation process: 1) we illustrate that in the absence of the biofilm our numerical simulation converges to the analytical solution; 2) we verify that our multigrid technique is correctly accelerating the convergence of our chosen relaxation scheme; and 3) we determine the convergence rate of the simulations with a biofilm using a mesh refinement convergence analysis.

Before discussing the results of our validation process, we provide a brief description of the two primary sources of error present in our simulations, 4.1. We also setup our simulations with a detailed description of

initial Lagrangian node positions in 4.2. Then we provide 2D simulation validation in 4.3 and 3D validation in 4.4.

4.1. Discussion of Errors

In our numerical scheme, we have two sources of error: 1) *discretization error* is introduced by discretizing the Navier-Stokes equations in space and time; and 2) *algebraic error* is introduced when we attempt to solve the resultant systems of linearized equations.

As it is impossible to compute the true algebraic error, we use the norm of the residual to deduce an upper bound on the algebraic error using Equation (31). Recall that Equation (31) indicates that the relative algebraic error at each timestep is no larger than the condition number of the matrix times the relative residual norm (recall that $\frac{\|r\|}{\|f\|}$ is the relative residual norm). We do not construct these matrices during the actual simulations because we do not need them to solve the systems. However, we did construct them to find their condition numbers and found that the condition numbers for the matrices used in the computations for $\tilde{\mathbf{u}}^{n+1}$ and p^{n+1} are $O\left(h^{-2}\right)$ (this is true for both 2D and 3D simulations). The simulations that resulted in the plots given in 5.2 and 5.3 were run using $h = \frac{1}{128}$, and thus the matrix condition numbers were approximately 10^4.

Our goal in the simulations is to ensure that the algebraic error falls well below the discretization error at each time step, so the total error will be dominated by the discretization error. In theory, the discretization error is at best $O(h^2) \approx C\left(1/128\right)^2 \approx C \times 6 \times 10^{-5}$, for $C > 0$, with our discretization. Using a stopping criteria of 10^{-9} for the relative residual at each timestep should suffice (i.e., from (31)). We continue to the next time step only when the computed relative residual, $\frac{\|r^h\|}{\|f^h\|} \leq 10^{-9}$, because this implies $\|e^h\| \leq cond(A) * 10^{-9} \approx 10^{-5}$.

Another factor influencing the capability of our simulations is that after, extensive simulation, we discover that our linear solver is limited to converging to a relative residual norm of about 10^{-11} (possibly from machine precision issues). With $h = \frac{1}{512}$, the condition number is $O(10^5)$ and the discretization error is $O(10^{-6})$, so the algebraic error is at best bounded by about $10^{-11} \times 10^5 = 10^{-6}$ (see Equation (31)), and we can no longer be certain that the algebraic error falls below the discretization error at each timestep. For this reason, we restrict h to be larger than $\frac{1}{512}$ in all of the simulations and convergence analysis.

4.2. Simulation Setup

In these convergence simulations, we constructed an experimentally motivated mushroom shaped biofilm (shown in Figure 7 on page 19(a)). We carved this shape from a $1.6\,\mu$m slice cut from data points generated in the Younger and Solomon labs at the University of Michigan. These data points are 3D bacterial cell locations from 3D Leica SP2 confocal laser scanning microscopy images taken of *Staphylococcus epidermidis* RP62A (ATCC 35984) grown in a Stovall 3 channel flow cell for 24 hours at 37 C under a wall shear stress of 0.01 Pa. For further details of how the coordinates were computed, see Stewart et al. [41].
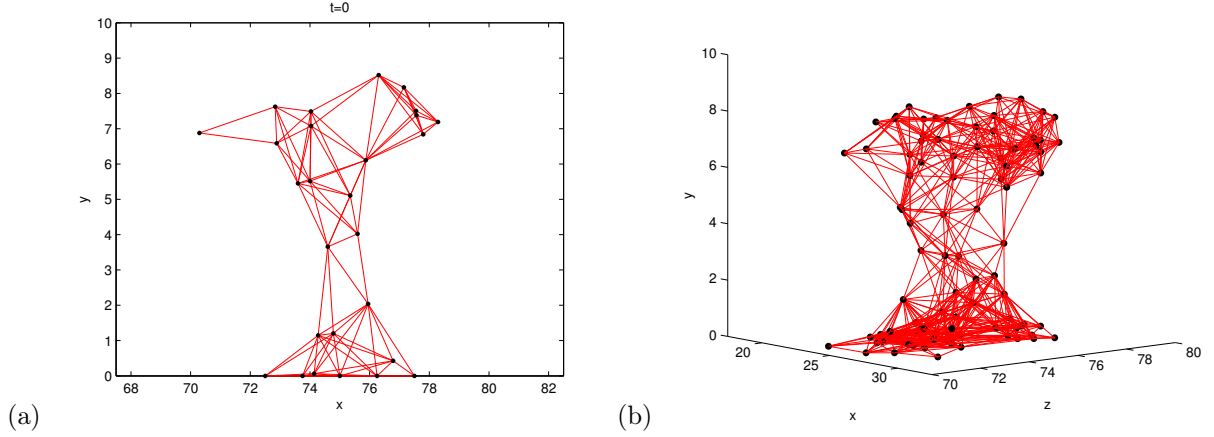
Figure 7: Mushroom-shaped biofilm at $t = 0$ in the middle of the computational domain attached to the bottom ($y = 0$) of the tube. (a) This is the shape used in the 2D simulations, and (b) 3D mushroom shaped biofilm at $t = 0$.

From this data, the average Lagrangian volume element, d_0^3, is calculated to be approximately $4.036\,\mu\mathrm{m}^3$, and thus we use $d_0 = 1.59\,\mu\mathrm{m}$ in both the 2D and 3D simulations. We connect the initial distribution of cells with a distance based connection criteria. Our inspiration for the connection distance criteria came from the closeup images of biofilms such as the one shown in Figure 1 on page 3. We observed that each bacterial cell is connected to neighboring cells that are within about $2d_0$. Thus, we varied the connection criteria in our algorithm between 1.5-$2.5 \times d_0$ in an effort to find one that resulted in a biofilm that was sufficiently connected but not overcrowded. This resulted in the choice of a connection criteria of $d_c = 2.8\,\mu\mathrm{m}$. In other words, we placed spring connections between Lagrangian nodes at the beginning of the simulation with every node connected to every other node less than $2.8\,\mu\mathrm{m}$ away. Admittedly, this value of d_c is arbitrary, and future work will include deriving a method to determine this connection criteria through image analysis of closeup images of biofilms similar to Figure 1 on page 3. The mushroom shaped biofilm has a height of about $8.5\,\mu\mathrm{m}$ and width of about $8\,\mu\mathrm{m}$ (see Figure 7 on page 19). In the convergence simulations, the maximum spring force, F_{max}, is set to $5 \times 10^{-6}\,\mathrm{N}$. The fluid parameters for these convergence simulations are provided later in Table 9 on page 28.

Note that $\tilde{\delta}$ is a function of ω, a scaling parameter we must choose that determines the volume/area of influence when the forces and density are transferred to the Eulerian grid. We must also point out here that a more accurate representation of the Dirac delta function occurs when $\omega \geq h$. Thus, for the purpose of the convergence simulations, we use $\omega = 1.0\,\mu\mathrm{m}$ in the transfer equations, (9) and (10). However, in our simulations, we use $\omega = 0.5\,\mu\mathrm{m}$ since the actual radius of *Staphylococcus epidermidis* is known to be about $0.5\,\mu\mathrm{m}$ [43]. Using a characteristic length of $L = 50\,\mu\mathrm{m}$, we have the non-dimensionalized $\omega^* = \frac{\omega}{L} = \frac{1}{50}$. Dropping the star from the dimensionless variable, we use $\omega = \frac{1}{50}$ in the convergence simulations and $\omega = \frac{1}{100}$ in the results simulations. We desire that $\omega \geq h$, so that the Lagrangian forces are spread at least two Eulerian mesh widths in every direction (as is done in the traditional IBM [30]). Using $\omega = \frac{1}{50}$ in the
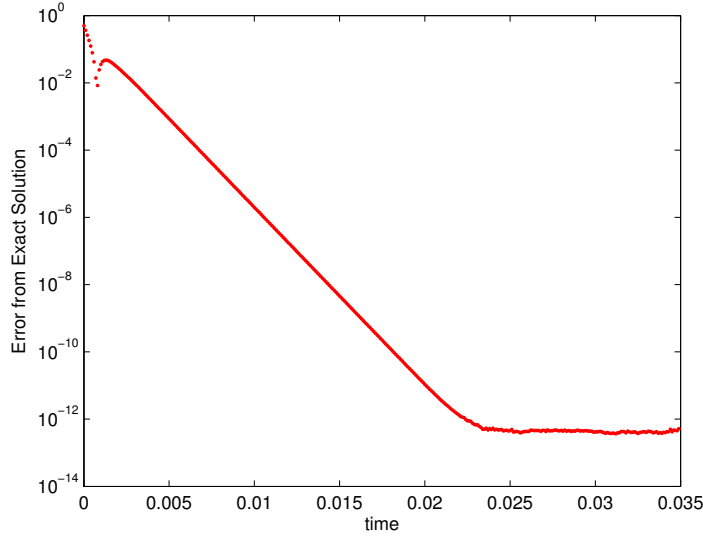
Figure 8: Exact error in biofilm-free 2D simulation with $h = \frac{1}{128}$. The solution is compared to the exact solution, (32), using a maximum norm.

convergence simulations allows $h = \frac{1}{64}, \frac{1}{128}, \frac{1}{256}$ to obey these criteria. We again note that one of the reasons for using ω in the scaling of (14) as opposed to h is that better spatial convergence rates are achieved since the scaling is independent of h.

4.3. Two-Dimensional Validation

In the absence of a biofilm, we expect that using a centered finite difference approximation for the second derivatives allows *exact* convergence to the second-order polynomial solution (Equation (32)). That is to say, we expect the numerical solution to converge to the analytical within machine precision. Reassuringly, we find that the biofilm-free simulations converge exactly to the steady state laminar flow.[4] To illustrate, we started with an initial velocity profile that is one-half of that of the laminar flow velocity profile. The error in the simulation converged (within machine precision) in less than 300 time iterations for all spatial resolutions (see Figure 8 on page 20 for example with $h = 1/128$ and $dt = 0.0001$).

4.3.1. Multigrid performance

Next, we provide numerical evidence that the multigrid technique convergences optimally to the solutions of (27) and (30). Define a *work unit* as the cost of performing one relaxation on the finest grid (see [7]). In Figure 9 on page 21(a), we depict (for the pressure computation) the work units required to reach the minimum residual error as a function of allowed levels in the multigrid. This result shows that the number of work units required decreases significantly with each added multigrid level. This means that the multigrid

---

[4]In the 3D simulations, we do not see exact convergence since the laminar solution is not a second-order polynomial. See 5.3 for details on the convergence properties of the 3D laminar flow case.

method correctly accelerates the convergence of our iterative method by doing computations on the coarser grids. For example, with just one allowed level of multigrid, the relaxation uses only the finest resolution grid and requires about 10^5 work units, whereas with 6 multigrid levels we only require about 10^2 work units to achieve the same error. Note that there is no reduction in the number of required work units with the addition of a 7th level in the multigrid, so we use at most 6 levels in our 2D solvers. The data in this plot was obtained using our 2D simulation with a mushroom shaped biofilm similar to those shown in 5.2.
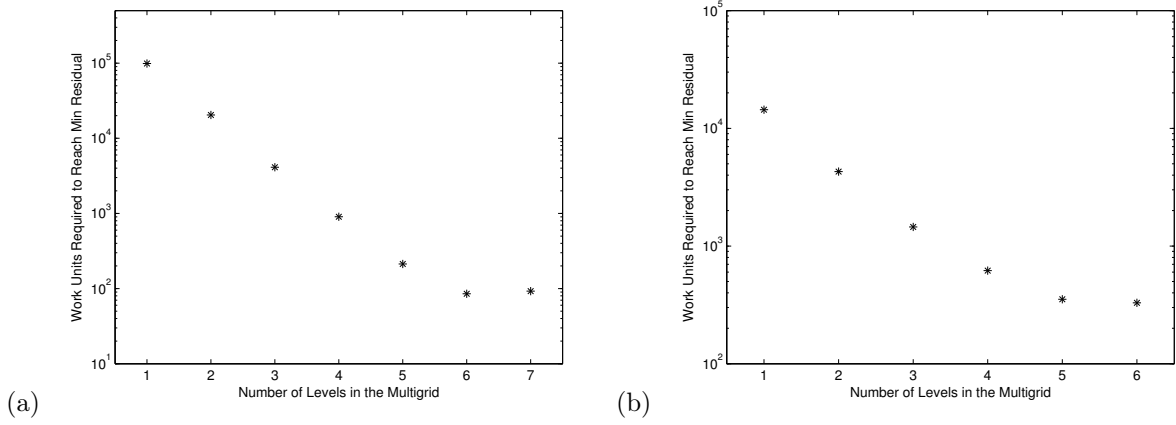

Figure 9: Decrease in work units required to reach the minimum residual error as the number of multigrid levels is increased in the (a) 2D simulations, (b) and 3D simulations.

4.3.2. Empirical Estimate of Convergence Rate in Time

Similar to the development by Mori and Peskin in [25], we define a measure of error by

$$E_p(q(T); \Delta t) = \left\| q^{\Delta t}(T) - q^{\Delta t/2}(T) \right\|_p, \tag{37}$$

which is the error difference at time $t = T$ in a computed quantity, q, using a temporal refinement of a half timestep. Then, an *empirical estimate* for the convergence rate is calculated using

$$r_p(q(T); \Delta t) = \log_2 \left(\frac{E_p(q(T); \Delta t)}{E_p(q(T); \frac{\Delta t}{2})} \right). \tag{38}$$

We compute the approximate convergence rate in time using the E_2 and E_∞ errors in the Eulerian variable, **u**, and in the Lagrangian variable, **X**. We simulate until $t = T = 0.01$ s using temporal step sizes that ranged from $\Delta t = 1/5000$ to $\Delta t = 1/80000$, decreasing by a factor of 2 at each level. The Eulerian grid is discretized with a step size of $h = 1/256$.

The empirical convergence rates from our temporal refinement are provided in Table 1 on page 23. The immersed boundary method, as we have implemented it, is formally second-order in space and first order in time, but, for problems with sharp interfaces that do not have smooth solutions, it is limited to first-order accuracy in space and time. Thus for our problem we expect only first order accuracy. The convergence

21

rates in time given in Table 1 on page 23 show first-order convergence in time as is expected. In Figure 10 on page 23(a), we depict the exact values of $E_p(q(T); \Delta t)$ for $q = \mathbf{X}$ and $q = \mathbf{u}$. We show $\log_2$ in the x and y axes so that the empirical convergence rates from Table 1 on page 23 appear as the slope of the line segments.

4.3.3. Empirical Estimate of Convergence Rate in Space

For this refinement study, we define a measure of error by

$$E_p(q(T); h) = \left\| q^h(T) - I_h^{2h}\left(q^{h/2}(T)\right) \right\|_p, \tag{39}$$

which is the error difference at time $t = T$ in a computed quantity, q, using a spatial refinement of a half. In this definition, I_h^{2h} is the restriction operator from a fine to a coarse grid. Then, an empirical estimate for the convergence rate is calculated using

$$r_p(q(T); h) = \log_2\left(\frac{E_p(q(T); h)}{E_p(q(T); \frac{h}{2})}\right). \tag{40}$$

We note that the estimates for convergence rates given by (38) and (40) have a fairly simple derivation using a Taylor series expansion (see [13] or [21]).

In the spatial refinement analysis, we did not refine the Lagrangian grid with the Eulerian grid, so the same number of Lagrangian points were present in all of the simulations. In addition, full weighting restriction is used in the definition of the error, (39), for the error in $\mathbf{u}$. We also used a fixed timestep of $\Delta t = 10^{-4}$ until $t = T = 0.01\,\mathrm{s}$ for all of these simulations. The computed convergence rates from this refinement are provided in Table 2 on page 23. The ∞-norm convergence rates given in Table 2 on page 23 show greater than first-order convergence in space for the error in the Lagrangian variable $\mathbf{X}$ and in the Eulerian variable $\mathbf{u}$. The seemingly large convergence rates for the lower resolution grids ($h = \frac{1}{16}, \frac{1}{32}, \frac{1}{64}$) can be explained by the fact that using $\omega = \frac{1}{50}$ in the Dirac delta approximations does not allow the Lagrangian forces to be adequately represented in the Eulerian grid. This leads to larger errors in the coarse-grid simulations. Therefore, the best estimates for the convergence rates are the ones using the three resolutions all obeying $\omega > h$ given in the 4th and 7th columns of Table 2 on page 23. In Figure 10 on page 23(b), we depict the exact values of $E_p(q(T); h)$ for $q = \mathbf{X}$ and $q = \mathbf{u}$. We show $\log_2$ in the x and y axes so that the empirical convergence rates from Table 2 on page 23 appear as the slope of the line segments. We discuss possibilities for improvement in the convergence rates later in the conclusion sections.

We also used a grid refinement analysis to find the empirical convergence rate with spatial refinement when the density of the biofilm is two times that of the surrounding fluid. This analysis was done to show that the first order convergence rate is maintained with the increased density in the biofilms. The results of this convergence analysis are shown in Table 3 on page 24 and Figure 10 on page 23(c).

Finally, we compute the empirical convergence rates for our 2D simulation with variable viscosity. In this convergence study, (Table 4 on page 24 and Figure 10 on page 23(d)) we use a non-dimensionalized

value of biofilm viscosity of $\mu_{max} = 500$, which means that the viscosity at the location of a Lagrangian node is 500 times that of the surrounding fluid. First-order convergence in space is maintained, even with this very large biofilm viscosity.
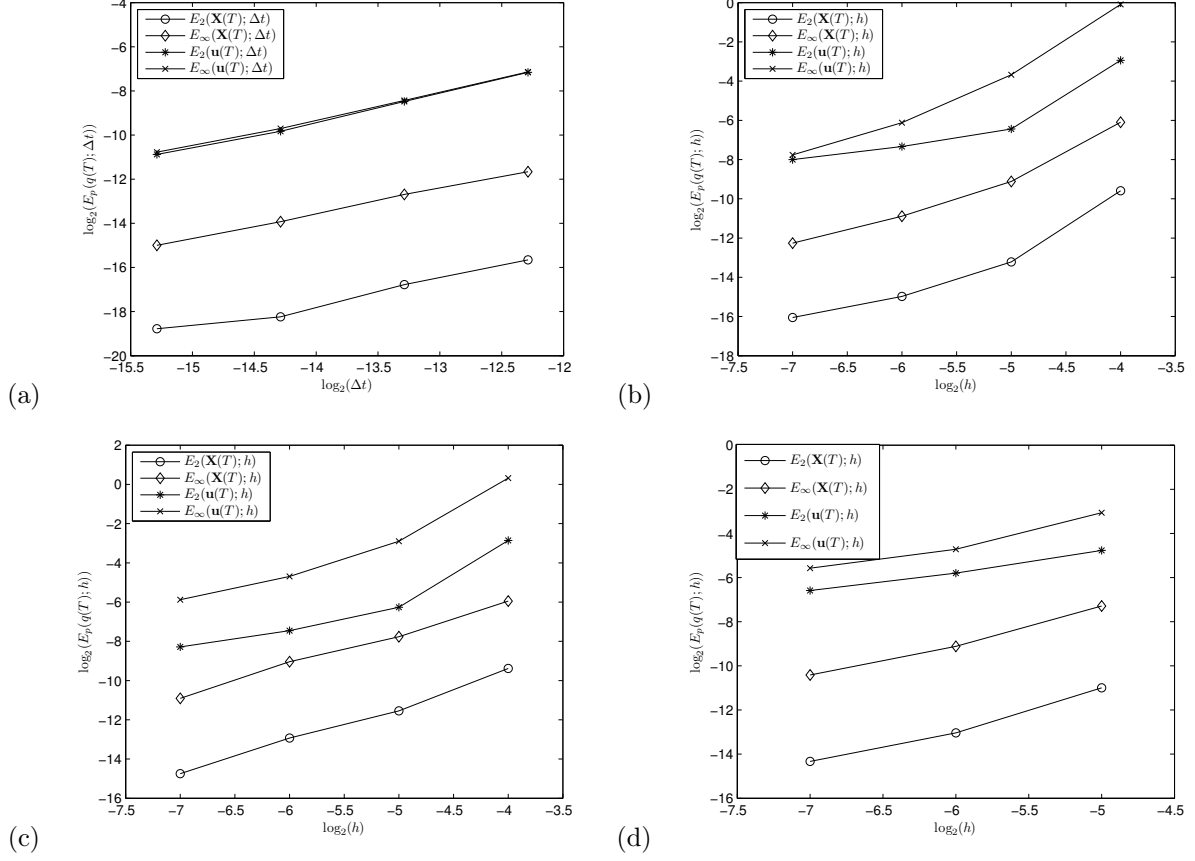

Figure 10: Empirical error estimates with (a) temporal refinement: $E_p(q(T); \Delta t)$ is the p-norm of the error as defined by (37), (b) spatial refinement with constant density and viscosity: $E_p(q(T); h)$ is the p-norm of the error as defined by (39), (c) spatial refinement and increased biofilm density, (d) spatial refinement and increased biofilm viscosity. In all plots, we show $\log_2$ in the x and y axes so that the empirical convergence rate appears as the slope of the line segments.

q	$r_2(q(T); .0002)$	$r_2(q(T); 10^{-4})$	$r_2(q(T); \frac{10^{-4}}{2})$	$r_\infty(q(T); .0002)$	$r_\infty(q(T); 10^{-4})$	$r_\infty(q(T); \frac{10^{-4}}{2})$
u	1.32	1.31	1.08	1.29	1.28	1.07
X	1.12	1.45	0.54	1.04	1.23	1.07

Table 1: Empirical convergence rates with temporal refinement. $r_p(q(T); dt)$ is the convergence rate in the variable, q, at $t = T$ using the p-norm and the three time steps dt, $dt/2$, $dt/4$.

q	$r_2(q(T); \frac{1}{16})$	$r_2(q(T); \frac{1}{32})$	$r_2(q(T); \frac{1}{64})$	$r_\infty(q(T); \frac{1}{16})$	$r_\infty(q(T); \frac{1}{32})$	$r_\infty(q(T); \frac{1}{64})$
u	3.51	0.89	0.65	3.59	2.44	1.65
X	3.62	1.80	1.07	3.02	1.77	1.37

Table 2: Empirical convergence rates with spatial refinement. $r_p(q(T); h)$ is the convergence rate in the variable, q, at $t = T$ using the p-norm and the three Eulerian step sizes h, $h/2$, $h/4$.

q	$r_2(q(T); \frac{1}{16})$	$r_2(q(T); \frac{1}{32})$	$r_2(q(T); \frac{1}{64})$	$r_\infty(q(T); \frac{1}{16})$	$r_\infty(q(T); \frac{1}{32})$	$r_\infty(q(T); \frac{1}{64})$
u	3.42	1.19	0.84	3.23	1.79	1.20
X	2.20	1.38	1.82	1.83	1.26	1.88

Table 3: Empirical convergence rates with spatial refinement and increased biofilm density. $r_p(q(T); h)$ is the convergence rate in the variable, q, at $t = T$ using the p-norm and the three Eulerian step sizes h, $h/2$, $h/4$. In this experiment, the density of the biofilm is double that of the surrounding fluid.

q	$r_2(q(T); \frac{1}{32})$	$r_2(q(T); \frac{1}{64})$	$r_\infty(q(T); \frac{1}{32})$	$r_\infty(q(T); \frac{1}{64})$
u	1.04	0.78	1.67	0.86
X	2.04	1.29	1.82	1.31

Table 4: Empirical convergence rates with spatial refinement and increased biofilm viscosity. $r_p(q(T); h)$ is the convergence rate in the variable, q, at $t = T$ using the p-norm and the three Eulerian step sizes h, $h/2$, $h/4$. In this experiment the viscosity of the biofilm is 500 times that of the surrounding fluid.

4.3.4. Time-Step Stability Restrictions

Finally, we investigated the stability of the method computationally as it depends on the spatial and temporal refinement and the stiffness of the springs. Analytically, stability applies to a numerical scheme and not to a computational run, but here we follow Mori and Peskin in [25] and give a simple definition of the stability for each computational run. Using the square of the 2-norm defined by (36) on **u** (i.e. $\|\mathbf{u}\|_p^2$) gives a value which is proportional to the kinetic energy in the system. We call the simulation *stable* if magnitude of the total velocity (as measured by the total kinetic energy) does not have a time of extreme growth during the simulation. Moreover, this kinetic energy should remain relatively close to the value of the total kinetic energy in the case of no biofilm. Using this definition of stability, we found, through experimentation with many combinations of h, Δt, and F_{max}, that we have timestep restrictions that scale with the mesh-width, h, and with the maximum Lagrangian force, F_{max}. The restrictions are approximately given by

$$\triangle t \leq C_1 h$$

and

$$\triangle t \leq \frac{C_2}{F_{max}},$$

where C_1 and C_2 are positive proportionality constants. Specific values of C_1 and C_2 change depending on the parameters of the simulation. In future simulations, we hope to avoid these timestep restrictions by using an implicit or semi-implicit method as is done in [25] and [26]. All of the simulations shown in this work and used in the convergence testing used time-steps satisfying these two restrictions.

4.4. Three-Dimensional Validation

In this subsection, we provide some numerical evidence validating the 3D simulations. We first validate in the absence of a biofilm using the exact laminar flow solution. Then, we validate the multigrid method in the presence of a biofilm and, finally, we provide the empirical convergence rates for the simulation in the presence of a biofilm.

We first tested the rate of convergence of our method on the laminar flow case without the interference of a biofilm. To illustrate the convergence rate in the absence of a biofilm, we started with an initial velocity profile that is one-half of that of the laminar flow velocity profile, given by (34). We ran the simulation enough timesteps until the approximate solution converged, with only discretization error remaining, to the exact solution for six spatial step sizes, $h = \left\{\frac{1}{4}, \frac{1}{8}, \frac{1}{16}, \frac{1}{32}, \frac{1}{64}, \frac{1}{128}\right\}$. We computed the discretization error (using the exact laminar solution, (34), for computations) for each of the step sizes and found that the error is $O(h^2)$. This can be seen in Figure 11 on page 25, where on the vertical axis we have the $\log_2$ of the error so that the convergence rate appears as the slope in the plot.

Next, in Figure 9 on page 21(b), we depict (for the pressure computation) the work units required to reach the minimum residual error as a function of allowed levels in the multigrid approach. This again implies that the multigrid method correctly accelerates the convergence of our iterative method for the 3D simulations with a biofilm. Note that there is only a slight reduction in the number of required work units with the addition of a 6th level in the multigrid, and we saw no reduction with 7 levels, so we use at most 6 levels in our 3D solvers.
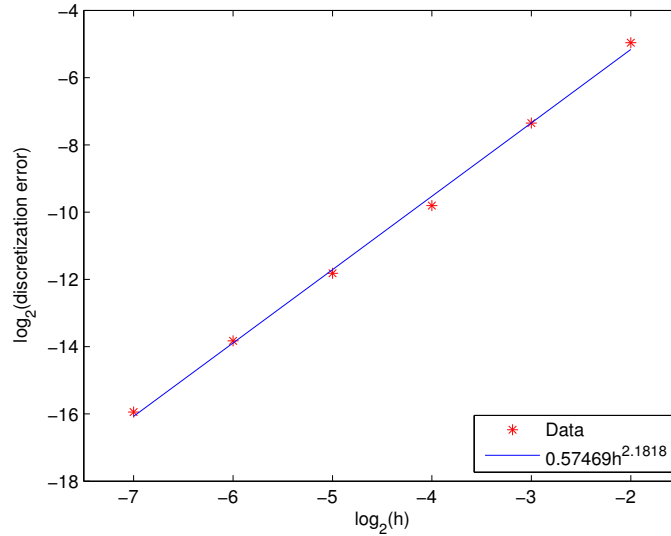

Figure 11: We show the convergence rate in the laminar flow case. These points are discretization errors for each of the spatial step sizes ($\frac{1}{4}$, $\frac{1}{8}$, $\frac{1}{16}$, $\frac{1}{32}$, $\frac{1}{64}$, $\frac{1}{128}$).

Finally, as was done for the 2D case in 4.3.3, we compute the empirical convergence rates for our 3D simulation in the presence of the biofilm shown in Figure 7 on page 19(b) with all of the same fluid parameters used in the 2D analysis. Using the p-norms defined above, we can compute the convergence rates using (38) and (40) (see Figure 12 on page 26(a) and Table 5 on page 26). For the temporal convergence analysis, we used $\omega = \frac{1}{50}$ and $h = \frac{1}{64}$. This analysis resulted in first-order convergence in all measures except $r_p(q(T); \Delta t)$ in which it has an average convergence rate of about 0.6. Next, we found empirical convergence rates for

spatial refinement (see Table 6 on page 27 and Figure 12 on page 26(b)). As expected, we observe a greater than first-order convergence rate in both the Eulerian velocity, $\mathbf{u}$, and the Lagrangian position, $\mathbf{X}$. Next, we conducted a spatial refinement analysis with a biofilm that has double the density of the surrounding fluid (see Table 7 on page 27 and Figure 12 on page 26(c)). Finally, we did the spatial refinement study for our simulations with $\mu_{max} = 500$, and again achieved first-order spatial convergence (see Table 8 on page 27 and Figure 12 on page 26(d)).
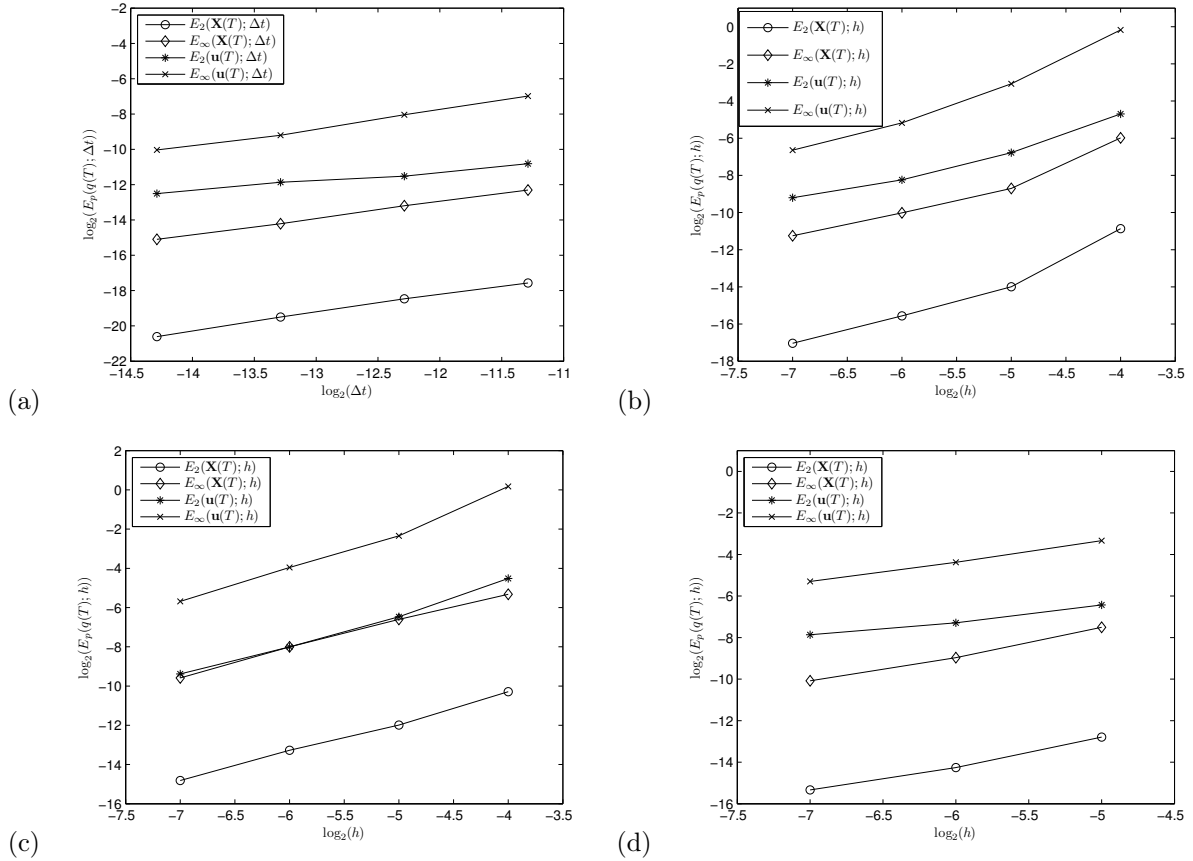

Figure 12: Empirical errors in the 3D simulations with (a) temporal refinement: $E_p(q(T); \Delta t)$ is the p-norm of the error as defined by (37), (b) spatial refinement with constant density and viscosity: $E_p(q(T); h)$ is the p-norm of the error as defined by (39), (c) spatial refinement and increased biofilm density, (d) spatial refinement and increased biofilm viscosity. We show $\log_2$ in the x and y axes so that the empirical convergence rate appears as the slope of the line segments.

q	$r_2(q(T); .0004)$	$r_2(q(T); .0002)$	$r_2(q(T); 10^{-4})$	$r_\infty(q(T); .0004)$	$r_\infty(q(T); .0002)$	$r_\infty(q(T); 10^{-4})$
$\mathbf{u}$	0.71	0.35	0.64	1.04	1.18	0.83
$\mathbf{X}$	0.90	1.03	1.11	0.90	1.02	0.88

Table 5: Empirical convergence rates in the 3D simulations with temporal refinement are shown for $\mathbf{u}$ and $\mathbf{X}$. $r_p(q(T); \Delta t)$ is the convergence rate in the variable, q, at $t = T$ using the p-norm and the three Eulerian step sizes Δt, $\Delta t/2$, $\Delta t/4$.

q	$r_2(q(T);\frac{1}{16})$	$r_2(q(T);\frac{1}{32})$	$r_2(q(T);\frac{1}{64})$	$r_\infty(q(T);\frac{1}{16})$	$r_\infty(q(T);\frac{1}{32})$	$r_\infty(q(T);\frac{1}{64})$
u	2.09	1.44	1.02	2.89	2.11	1.47
X	3.12	1.57	1.47	2.70	1.33	1.23

Table 6: Empirical convergence rates in the 3D simulations with spatial refinement are shown for **u** and **X**. $r_p(q(T);h)$ is the convergence rate in the variable, q, at $t = T$ using the p-norm and the three Eulerian step sizes h, $h/2$, $h/4$.

q	$r_2(q(T);\frac{1}{16})$	$r_2(q(T);\frac{1}{32})$	$r_2(q(T);\frac{1}{64})$	$r_\infty(q(T);\frac{1}{16})$	$r_\infty(q(T);\frac{1}{32})$	$r_\infty(q(T);\frac{1}{64})$
u	1.95	1.52	1.40	2.52	1.61	1.73
X	1.7	1.28	1.55	1.29	1.40	1.56

Table 7: Empirical convergence rates with 3D spatial refinement and increased biofilm density. $r_p(q(T);h)$ is the convergence rate in the variable, q, at $t = T$ using the p-norm and the three Eulerian step sizes h, $h/2$, $h/4$. In this experiment, the density of the biofilm is double that of the surrounding fluid.

q	$r_2(q(T);\frac{1}{64})$	$r_2(q(T);\frac{1}{128})$	$r_\infty(q(T);\frac{1}{64})$	$r_\infty(q(T);\frac{1}{128})$
u	0.86	0.57	1.04	0.92
X	1.47	1.07	1.48	1.09

Table 8: Empirical convergence rates with 3D spatial refinement and increased biofilm viscosity. $r_p(q(T);h)$ is the convergence rate in the variable, q, at $t = T$ using the p-norm and the three Eulerian step sizes h, $h/2$, $h/4$. In this experiment, the viscosity of the biofilm is 500 times that of the surrounding fluid.

This concludes our validation section, and we now present the results of our numerical simulations.

5. Simulations Results

In this section, we present the results of our numerical simulations. First, we briefly discuss the reality of elastic forces in biofilms. Then we provide 2D results in 5.2 and 3D results in 5.3.

5.1. Discussion of Elastic Maximum Force, F_{max}

We now provide a brief discussion of the physical reality of the values of F_{max} used in our simulations. The *cohesive strength*[5] in biofilms has been found experimentally to be highly heterogeneous, with repeated experimental measurements on the same biofilm yielding vastly different strength measurements. For example, 49 cohesive strength measurements taken on only two samples of *Staphylococcus epidermidis* yielded measurements between 61-5182 Pa [1]. These biofilms were grown on a 22 mm diameter disc rotating at 75 $^{rot}/_{min}$ so the fastest speed, ~ 86 mm/s, was at the perimeter of the disc (i.e. very slow flow growth conditions). The *adhesive*[6] and cohesive strengths have also been shown to vary significantly with changes in growth conditions such as flow rate and nutrient concentration. Changes in these growth conditions influence the amount of ECM production in the biofilm as well as the compactness of the biofilm, which has a direct effect on its strengths [10, 27, 9]. We note here that the required values we find for F_{max} for

---

[5]The cohesive strength is a measure of the forces that interconnect the biofilm's cells.
[6]The adhesive strength is a measure of the forces that connect a biofilm to the surface.

Parameter Values for the Simulations	
Tube Radius	$25 \times 10^{-6}\,\mathrm{m}$
Fluid Dynamic Viscosity	$1.0 \times 10^{-3}\,\mathrm{kg/m{\cdot}s}$
Fluid Density	$998\,\mathrm{kg/m^3}$
Maximum Fluid Velocity	$10^{-3}\,\mathrm{m/s}$

Table 9: The values of parameters used in the 2D simulations.

the biofilms to remain attached in our 2D and 3D simulations are consistent with the cohesive strength measurements provided in [1]. Since the diameter *Staphylococcus epidermidis* is about $1\,\mu$m, in 3D, we multiply the cohesive strengths by $1\,\mu$m^2 to get an approximation for the range of forces on the surface area of one cell. Using the range of 61-5182 Pa yields a range of forces from 6.1×10^{-11} N to 5.18×10^{-9} N. In 2D, we multiply the cohesive strengths by the cell diameter to get a rough approximation for the range of forces on the surface perimeter surrounding one cell. Using the range of 61-5182 Pa yields a range of forces from 6.1×10^{-5} N to 5.18×10^{-3} N. Our values for F_{max} are at the low end of these ranges. The actual strength of the biofilm is most likely larger than our F_{max} values since the positional data was from a biofilm that was not fragmenting in the flow conditions in which it was grown, and we used the same flow conditions our simulations. Thus, in order to see detachment under these flow conditions, we had to lower the value of F_{max}. We could alternatively increase the flow rate to necessitate a larger F_{max} requirement to avoid detachment. One eventual goal of this work is that, if the approximate value of F_{max} is known for a particular type of biofilm, then our simulations can be used to predict the flow rates required to break different shaped biofilms.

5.2. Two-Dimensional Simulations

In this section, we provide results from our 2D simulations, which represent a cross-section of a biofilm attached to the inside of a tube and subjected to fluid flow in a computational domain of $150\,\mu$m by $50\,\mu$m. The parameters for our simulations are given in Table 9 on page 28.

In all simulations, we implement a breaking condition on the springs of two times the rest length. The initial configuration for the biofilm in these simulations is shown in Figure 7 on page 19. The spring connections between Lagrangian nodes are put in place at the beginning of the simulation with every node connected to every other node less than d_c away (the reason for this connection distance is given above in 4.2). The mushroom shaped biofilm has a height of about $8.5\,\mu$m and width of about $8\,\mu$m (width of about $2\,\mu$m at the thinnest part) . We use a non-dimensionalized $\omega = \frac{1}{100}$ to match the radius of *Staphylococcus epidermidis* and choose $h = \frac{1}{128}$ in all of the simulations shown, so that $\omega > h$.

In the first simulation, the maximum spring force, F_{max}, is set to 5.00×10^{-7} N, and the results are provided in Figure 13 on page 30. The biofilm bends over in the flow, and the connections in the thin part of the biofilm break as they stretch too far. The streamlines in (b), (c), and (d) of Figure 13 on page 30 and in all of the other 2D simulation plots follow the trajectories given by the velocity field, **u**.

We point out that the values of the spring constants are well within physically realistic values (see the discussion in 5.1), although, in this work, we have chosen these values for the qualities they give to the simulations rather than experimental evidence of the elastic strength of biofilms. For example, in these 2D simulations, we investigated several simulation runs with various spring constants until we obtained those that exhibited the above described behaviors.

Next, we conducted a simulation of the same mushroom shaped biofilm with all of the same parameter values, but we gave the biofilm additional density of $\rho_b = 998\,\mathrm{kg/m^3}$ compared to the ambient fluid. We know this density is larger than what is seen in actual biofilms (at most 20% greater density than water [24, 37]), but we chose it to show an exaggerated example of increasing the biofilm density. These result is provided in Figure 14 on page 31(b) and illustrates that the added density essentially adds momentum to the biofilm. This additional momentum causes the biofilm to curl over into the slower flow region and thus prevents detachment.

Finally, we conducted a simulation of the same mushroom shaped biofilm with all of the same parameter values as the first simulation, but we increased F_{max} to $5.00 \times 10^{-6}\,\mathrm{N}$. The effect of these stronger springs is that the thin part of the biofilm does not stretch enough to break the connections. The result is depicted in Figure 14 on page 31(c). We can see from these simulations that either increasing the biofilm density or strengthening the springs causes similar results, but, with the increased density, the biofilm has more of a curling action.

In the next simulation, we use all of the same parameters described in the first simulation, with the addition that the biofilm has a $500\times$ larger viscosity than the surrounding fluid, so $\mu_{max} = 0.5\,\mathrm{kg/m \cdot s}$. Comparing simulation results illustrated in Figure 14 on page 31(d) and Figure 14 on page 31(a), which show the biofilm configurations just before detachment, we observe a longer time until detachment in the high viscosity case. This is the expected outcome of increasing the viscosity in the biofilm. We note here that we used $\omega = \frac{1}{100}$ in the equation for $\mu(\mathbf{x})$ in (22) because we wanted to spread additional viscosity over the same region that the elastic forces are spread to. We achieve an even longer detachment time in the simulation by widening the influence of additional viscosity by using, for example $\omega = \frac{1}{50}$.
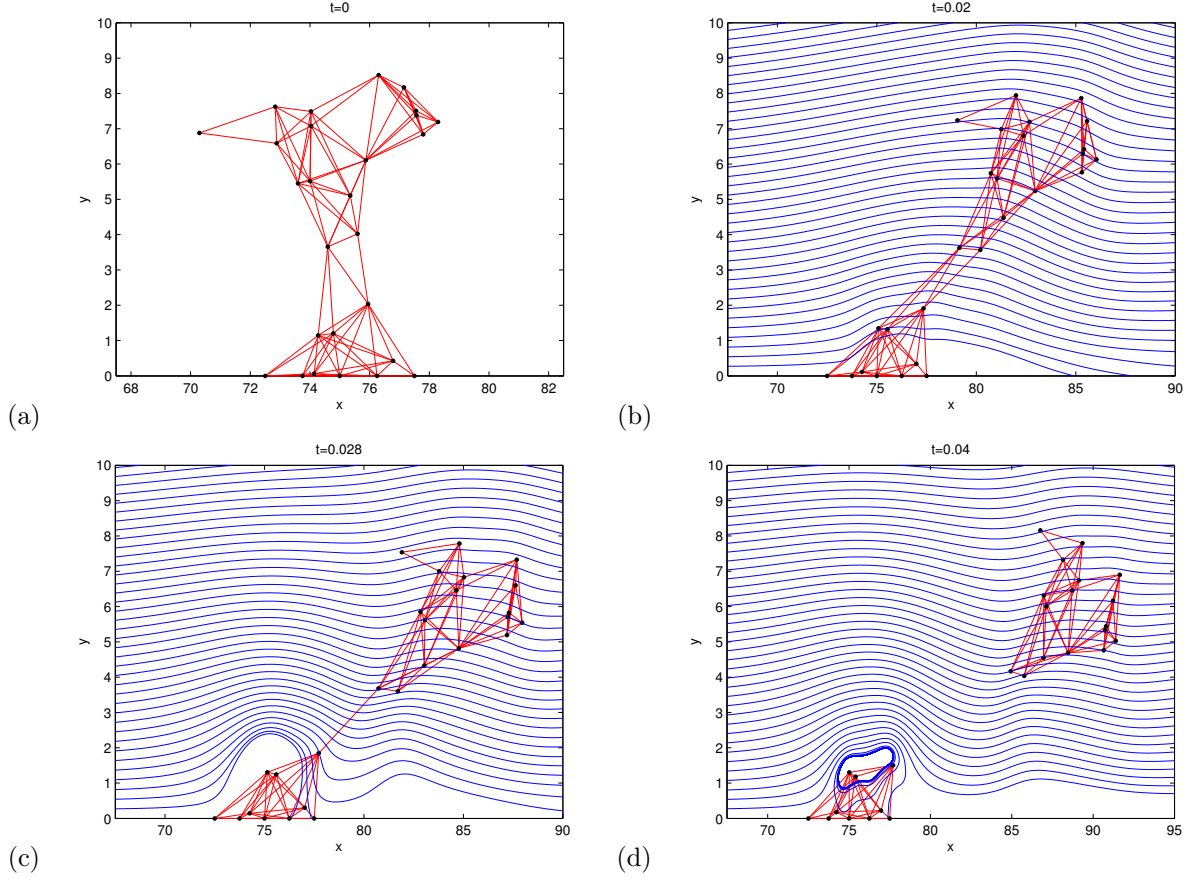
Figure 13: 2D Simulation of a mushroom shaped biofilm with the same density as the surrounding fluid. Time is in seconds and the distance is in microns. In this simulation, $\rho_0 = 998\,\mathrm{kg/m^3}$, $\rho_b = 0$, $F_{max} = 5.00 \times 10^{-7}\,\mathrm{N}$. The streamlines follow the velocity field. In this simulation, the top of the biofilm stretches in the flow, and the top breaks off as the connections in the the middle separate as they exceed the breaking criteria of twice the rest length. As expected in a laminar shear flow, the broken piece then tumbles end over end through the flow.
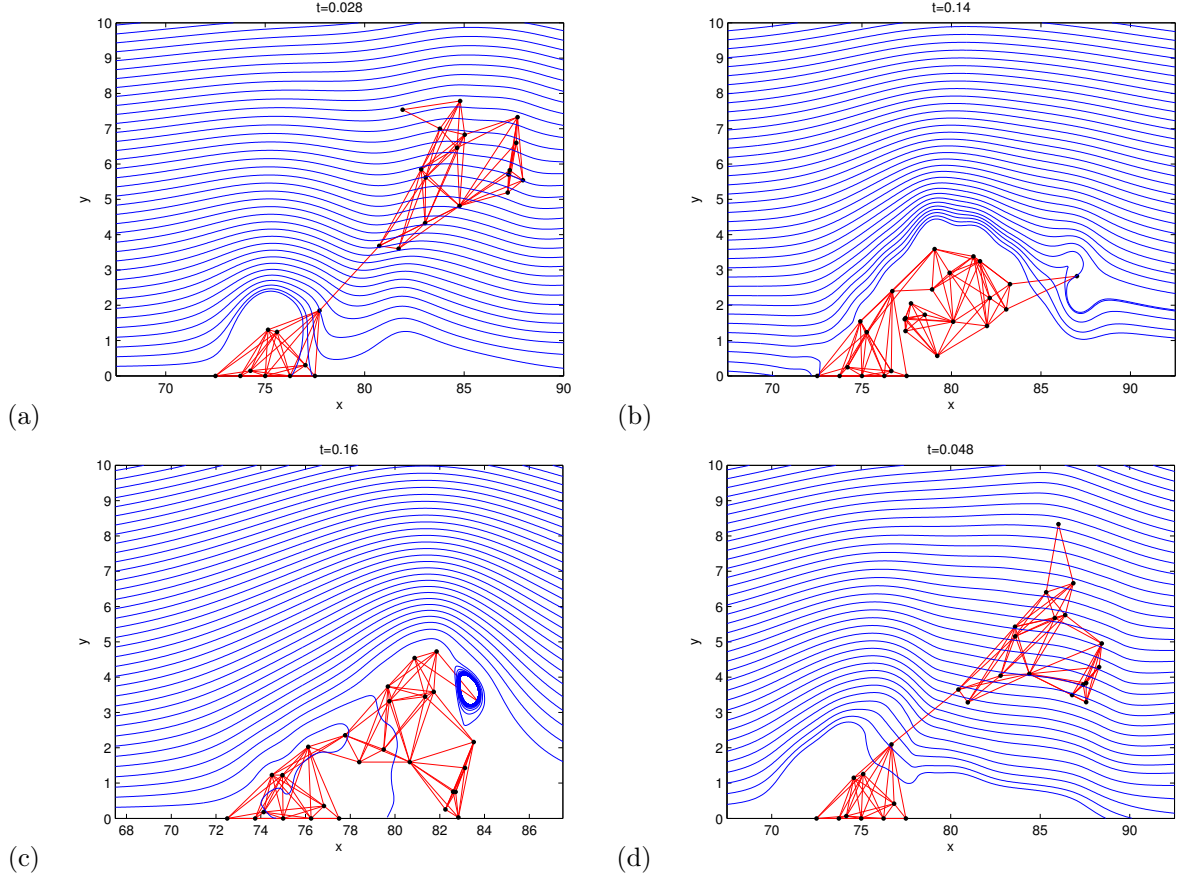
30

Figure 14: Snapshots of cell distributions resulting from 2D simulation of mushroom shaped biofilm with four different property configurations. In (a), the biofilm has the same density and viscosity as the surrounding fluid (just before detachment), (b) increased F_{max}, (c) density twice as large as the surrounding fluid density, and (d) viscosity is $500\times$ that of the surrounding fluid (just before detachment). The streamlines follow the velocity field.

5.3. Three-Dimensional Simulations

In this section, we provide results from our 3D simulations, which use the same parameter values as in the two dimensional simulations (see Table 9 on page 28). The difference is that the simulation in 3D represents flow through a square shaped tube with a side length of $50\,\mu$m. Note that these 3D simulations reproduce qualitatively the same results as in the 2D ones.

Our 3D simulations were run on a $50 \times 50 \times 150\,\mu$m computational domain. We simulate on a mushroom shaped biofilm with a height of about $8.5\,\mu$m and a diameter of about $7.5\,\mu$m. This shape is carved from the same set of data points described in 4.2. The spring connections between Lagrangian nodes are put in place at the beginning of the simulation, with every node connected to every other node less than $d_c = 3\,\mu$m away. Note that, for the 3D simulations, we increased d_c slightly to establish enough connections in the biofilm. We again use $\omega = \frac{1}{100}$ to match the radius of *Staphylococcus epidermidis* and choose $h = \frac{1}{128}$ in all of the simulations shown, so that $\omega > h$. In the first simulation, the maximum spring force, F_{max}, is set to $1.25 \times 10^{-12}\,$N. We again chose the value of these spring constants in order to illustrate specific

31

behaviors. The results of the first simulation are shown in Figure 15 on page 33. The mushroom shaped biofilm bends over and stretches in the flow. The connections in the midsection of the biofilm exceed their breaking length and the top of the biofilm breaks off into the flow. Next, we ran a simulation of the same mushroom shaped biofilm, but we added $\rho_b = 998\,\mathrm{kg/m^3}$ additional density to the biofilm compared to the surrounding fluid. The final result is provided in Figure 16 on page 34(b) and illustrates that the added density increases the momentum of the biofilm. This allows for the mushroom to curl over into the flow and increases the time until detachment. We also ran a simulation of the same mushroom shaped biofilm, but we increased F_{max} to $1 \times 10^{-11}\,\mathrm{N}$ and kept the biofilm density the same as the surrounding fluid. The result is provided in Figure 16 on page 34(c). The effect of these stronger springs is that the thin part of the biofilm does not stretch enough to break the connections. We can see from these simulations that either increasing the biofilm density or strengthening the springs causes similar results, but with the increased density the biofilm just curls over.

Finally, we provide one 3D simulation to show that, with increased biofilm viscosity, they produce qualitatively the same behavior as in the 2D case. In the simulation result shown in Figure 16 on page 34(d), we use the same parameters as the first 3D simulation, but we use a viscosity in the biofilm that is a factor of 500 times that of the surrounding fluid. Just as in the 2D case, this results in a longer time until detachment (compare time in Figure 16 on page 34(a) and Figure 16 on page 34(d)).

For ease of comparison, we now provide the figures in the order in which they were discussed in this section.
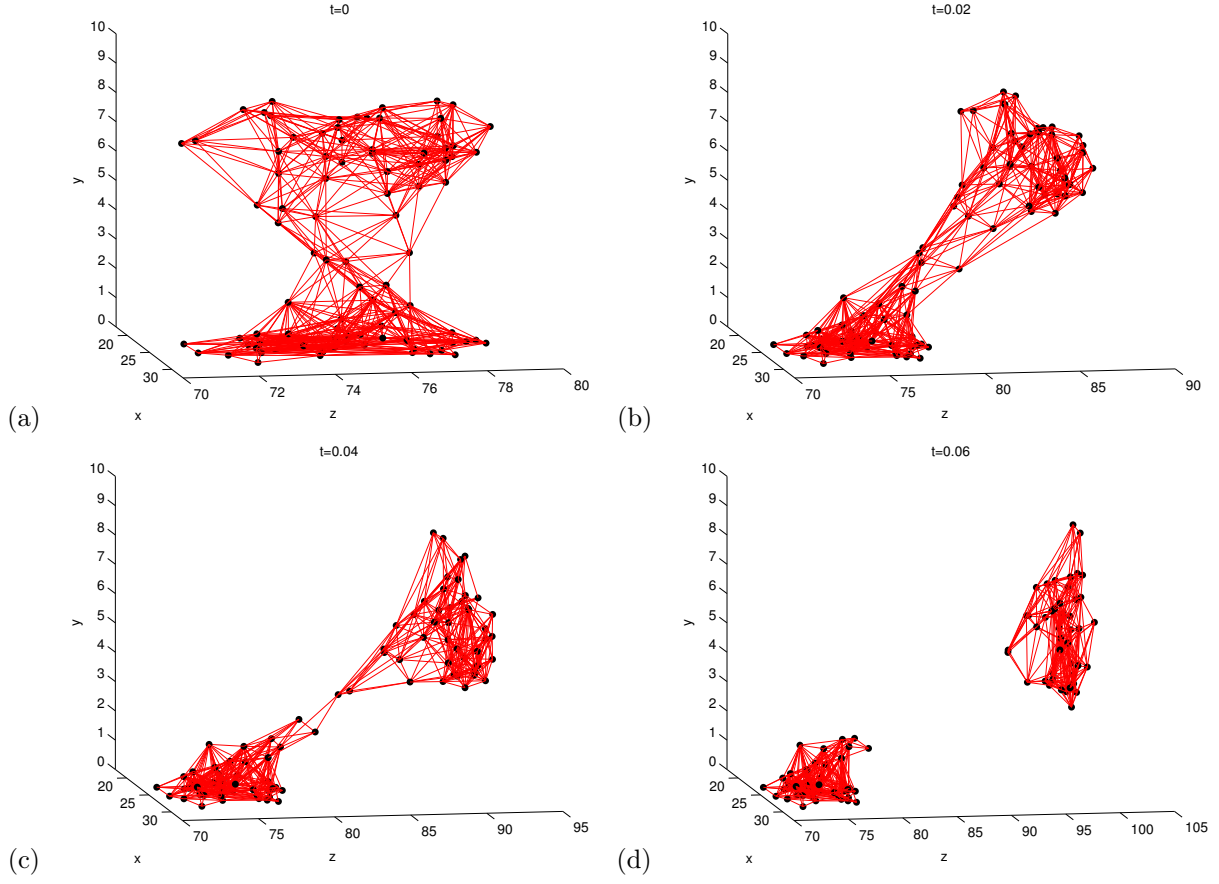
Figure 15: Full 3D simulation of a mushroom shaped biofilm with the same density as the surrounding fluid. The time is in seconds and the distance is in microns. As the biofilm stretches in the flow, the strain in the midsection exceeds the breaking length of the connections, and the top of the biofilm breaks off into the flow. Then the broken piece tumbles end over end through the flow, and the base retracts back. In this simulation, $\rho_0 = 998\,\mathrm{kg/m^3}$, $\rho_b = 0$, $F_{max} = 1.25 \times 10^{-12}$ N.
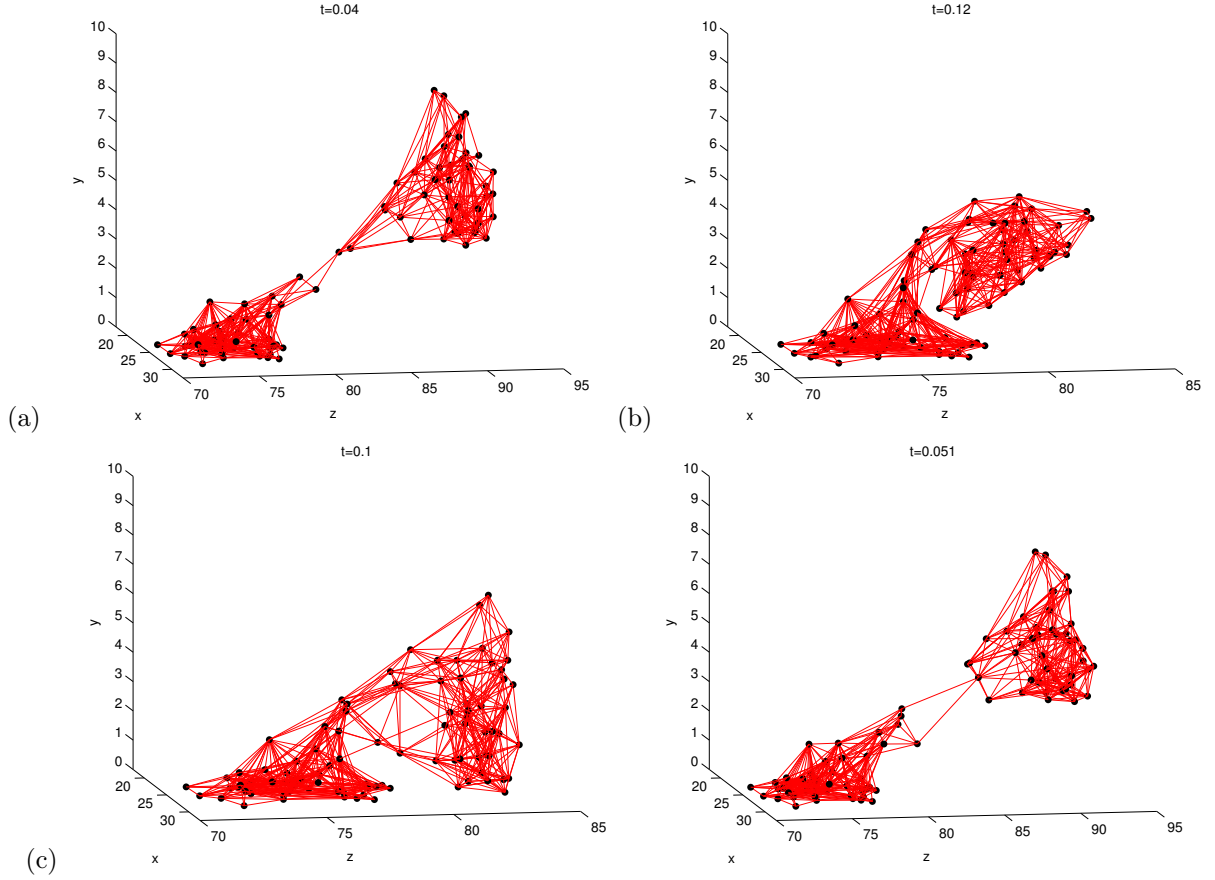
33

Figure 16: Snapshots of cell distributions resulting from 3D simulation of mushroom shaped biofilm with four different property configurations. In (a), the biofilm has the same density and viscosity as the surrounding fluid (just before detachment), (b) increased F_{max}, (c) density twice as large as the surrounding fluid density, and (d) viscosity is $500\times$ that of the surrounding fluid (just before detachment).

6. Realistically Shaped Biofilm Simulation

The biofilm shapes used in 5.2 and 5.3 were intentionally carved from the data in a way to provide a weak point at which it would be most likely to break. This was done in order to illustrate the effects of varying the different parameters in the simulation. In this section, we provide results of the simulation on a biofilm that is a subset of points taken directly from the real biofilm data set. In reality, this biofilm was surrounded by more cells on all sides, which would change the behavior of the fluid structure interactions. However, we use this to show the results of the simulation on a *real* top heavy biofilm shape that was grown in a lab. The *Staphylococcus epidermidis* data set discussed in 4.2 was supplied as positions in three $30 \times 30 \times 15 \,\mu$m sub-domains of a biofilm.

In Figure 17 on page 36(a), we show the biofilm taken from a $2 \times 30 \times 15 \mu$m subset of one data set that has been connected with $d_c = 2.8 \,\mu$m. For the 2D representation, we collapse the $2 \,\mu$m dimension, leaving only the (x, y) coordinates of the data. The most interesting feature of this biofilm is that in the region

from $x = 60\,\mu$m to $x = 67\,\mu$m the biofilm exhibits a mushroom shape similar to the one we used in 5.2.

We now provide two simulation results on this realistically shaped biofilm. The first simulation (see Figure 17 on page 36) uses a biofilm density equal to the surrounding fluid and uses $F_{max} = 7.5 \times 10^{-7}$ N. In this simulation, the mushroom shaped part pushes against the biofilm behind it, then rolls over the top of it as it breaks from its base, forming a long streamer-like biofilm.[7] Then the streamer breaks completely off leaving two distinct attached structures. In the second simulation, we use a biofilm density of $\rho_b = 120\,$kg/m³ and kept everything else the same. Although the density is only 12% larger than the surrounding fluid, it has a large impact on the outcome of the simulation. In this simulation, the effect of the increased density of the biofilm is a longer breaking time (compare time in Figure 18 on page 37(b) and Figure 18 on page 37(c)). This occurs since the increased momentum causes the first detached piece to continue further down, pulling the whole streamer lower (compare the height of the detaching pieces). The fluid forces continue to push the streamer until it breaks into the flow.

In the final simulation, we show that increasing the viscosity in the "realistically" shaped biofilm has larger impact on the results than in the case of the previous standalone mushroom shaped biofilm. In this simulation, we increased the biofilm viscosity to $50\times$ the surrounding fluid with $\mu_{max} = 0.05\,$kg/m·s. Although this is $10\times$ less than in the previous variable viscosity simulation, it has a larger impact on this wider biofilm, doubling the detachment time from the case of constant viscosity (compare Figure 18 on page 37(b) and Figure 18 on page 37(d)).

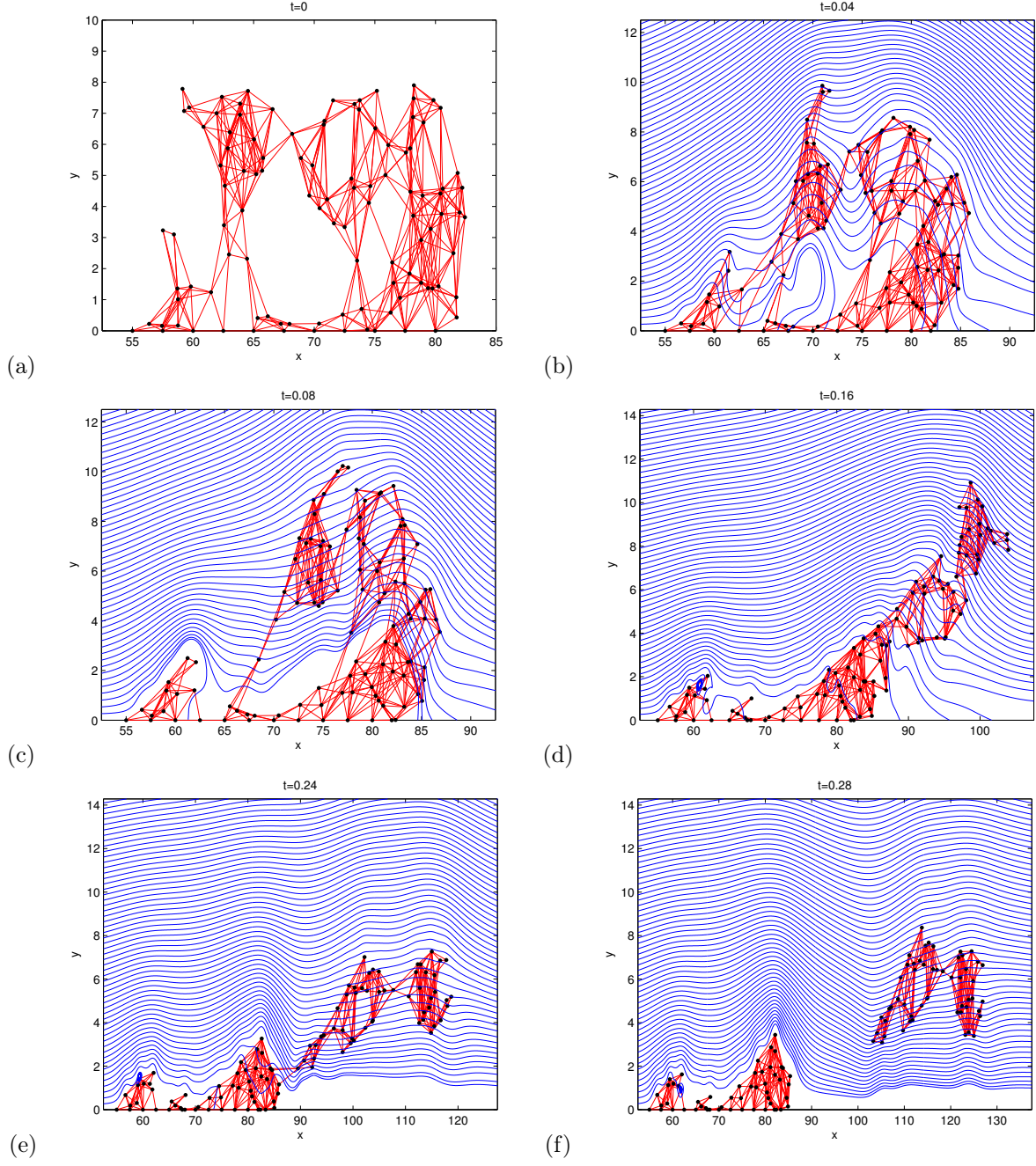[7] Streamers are a natural occurrence in biofilms. Examples in [17, 39].

Figure 17: Simulation on a 2D slice of a real biofilm with the same density as the surrounding fluid. Time is in seconds and the distance is in microns. In this simulation, $\rho_0 = 998\,\mathrm{kg/m^3}$, $\rho_b = 0$, $F_{max} = 7.5 \times 10^{-7}\,\mathrm{N}$. The streamlines follow the velocity field. In this simulation, the mushroom shaped part pushes against the biofilm behind it (b), then rolls over the top of it as it breaks from its base (d). Then a large portion of the biofilm breaks completely off leaving 2 distinct bases (f).
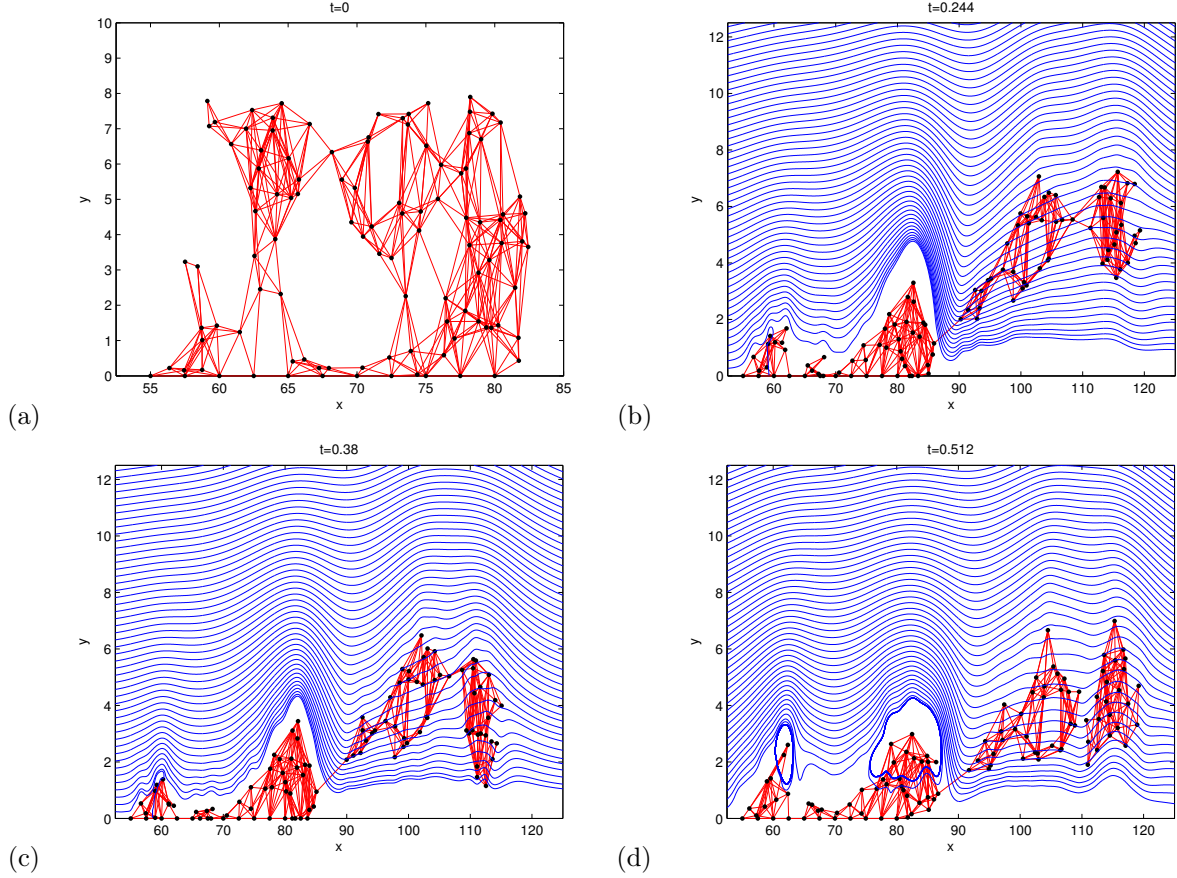
36

Figure 18: Snapshots in time showing the detachment time and configuration at detachment of a 2D slice of a real biofilm with initial configuration in (a). In (b), biofilm has the same density and viscosity as the surrounding fluid, (c) 12% larger density, and (d) 50× larger viscosity than the surrounding fluid. The streamlines follow the velocity field.

6.1. Numerical Concerns

We note that there remains one pressing concern that will be the focus of our future work. When adapting the multigrid scheme for large values of μ_{max}, we do not achieve expected speed ups in convergence rates. We use restriction to transfer the viscosity to the coarse grids works for small values of μ_{max}, but we found that, for larger values of μ_{max}, this technique leads to a very slowly converging solver. Intriguingly, we found that using our restriction operator to define the coarse grid viscous values and then scaling the values leads to faster convergence. Specifically, we define the coarse grid viscosity as

$$\mu_{lh}(\mathbf{x}) \quad = \quad \gamma_{lh} I_{\frac{1}{2}h}^{lh} \mu_{\frac{1}{2}h}(\mathbf{x}), \tag{41}$$

where lh denotes the grid whose mesh width is l times h ($l = 2, 4, 8, 16, \ldots$), $\gamma_{lh} \in (0, 1]$ is the scaling which maximizes the convergence of the solver, and $\mu_h(\mathbf{x})$ is defined by (22). Through repeated experimentation, we found that using $\gamma_{lh} \in [.7, 1]$ resulted in the fastest convergence rates in the 2D and 3D simulations. This approach is admittedly ad-hoc. However, the consistency with which we achieved dramatic speed ups strongly suggests the existence of an underlying mathematical principle to be discovered.

For our future work, the highest priority is to resolve the problem of slow convergence for large μ_{max}. There are three approaches that may lead to resolving this issue. The first would be to mathematically derive optimal values for the scaling parameters, γ_{lh}. Second, we could ensure that our discretization satisfies the Galerkin condition. Lastly, and probably the best choice, would be to re-implement the geometric multigrid as an algebraic multigrid method (AMG, see Ch. 8 of [7]).

7. Conclusions

In this work we developed a simulation to model the flow-induced fragmentation of biofilms. In this simulation, we have provided a way to adjust the biofilm density and viscosity, which had not been addressed in previous IBM biofilm models. We also have control of the fluid flow rate, density, viscosity, and elastic forces within the biofilm. We used experimentally measured biofilm bacterial cell locations as initial positions for our Lagrangian nodes. This is dramatically different than the traditional IBM, in which methods usually refine the Lagrangian mesh along with the Eulerian mesh. We adapted the Dirac delta approximation to scale with the radius of the bacteria rather than with the mesh width. This implies that the information that transfers from the Lagrangian grid to the Eulerian grid (i.e., density, viscosity, and elastic force) is spread over a set distance rather than scaling by the mesh width, h. This adapted Dirac Delta approximation improves our numerical convergence rates as well.

We used a projection method to split the incompressible Navier-Stokes equations to solve separately for an intermediate velocity and the pressure, and then used a Gauss-Seidel iterative method with multigrid to solve the resulting equations. Using an iterative solver, as opposed to a spectral method, to solve these systems was necessitated by the fact that biofilms have spatially varying density and viscosity. With this solver we achieved first order convergence in both space and time.

For the numerical simulations, we carved a mushroom shaped biofilm from the bacterial cell locations and ran simulations with varying parameters. We first ran the simulation on a simplistic shape in order to validate the effect of the various parameter changes on the outcome of the biofilm. By adjusting the maximum elastic force, F_{max} in the biofilm, we controlled the detachment phenomenon. We also showed that slight changes in the density of the biofilm has a large effect on the outcome of the simulation. This is an important conclusion as usually modelers ignore the differences in biofilm density. Finally, we showed that we can increase the detachment time in the simulations by increasing the viscosity of the biofilm. Finally, we ran simulations on more realistically shaped biofilms, which showed how a larger biofilm with different shapes will react to fluid flow forces. Adjusting these parameters will be a necessary component when we attempt to match these simulations to experimental data.

8. Future Work

There are several directions in which we plan to take this research in the future. For example, there are straightforward ways to include more biologically realistic terms to interpret biofilm internal stress dynamics, cell volume, and fragmentation dynamics. Additionally, there are approaches that may greatly improve our numerical scheme convergence and stability, including alternative multigrid algorithms, implicit discretizations, and improved immersed boundary implementations.

In its current form, our simulations could be used to make predictions in detachment times of biofilms, as well as general behavioral responses of biofilms to various flow conditions. We plan to work closely with experimentalists to formulate accurate viscoelastic models for the biofilms and modify our constitutive equations for stress and elasticity to account for these model choices. We also plan to include the fact that bacterial cells displace fluid. While we have adapted the Dirac delta function approximation to transfer the cell parameters (F, ρ, μ) to the Eulerian grid, the current simulation does not actually assign a size to the cells. As a result, the cells are free to pass through each other. We first plan to alter the model for the bacterial cell so that it displaces fluid. An important step in this process will be to identify a collision detection strategy. We will base ours on potentials for electrostatic, steric, and Van der Waals forces.

Our current simulation uses a spring-breaking criteria of double the rest length, and we also assume that the bonds are linearly elastic until the breaking point. This is not an accurate assumption, as it is known that biofilms are composed of polymer based ECMs. These structures are linearly elastic for small strains and then experience plastic deformation (permanently altering the bonds in the ECM and thus the rest length) before finally fracturing. In the future, we will use biofilm yielding data from experiments such as [1] to determine accurate approximations for yield points and fracture points in the biofilm. We plan to include plasticity into the simulations by changing the equations for stress, (20), when the bond has been stretched beyond its yield point.

We have several plans for improving our numerical method. Our current simulation is limited to first-order accuracy. Guided by the results in [8], we will accurately derive the numerical boundary conditions for our projection method to ensure second order accuracy for both velocity and pressure computations. To improve the accuracy of the immersed boundary method, we could also adapt our modeling method to either an immersed interface method ([22]) in which we adapt the finite difference approximations close to the interface or a blob projection immersed boundary method as discussed in [11] in order to obtain second-order spatial accuracy. Another limitation of our current numerical scheme is the time-step stability restrictions, which limit the size of the elastic forces between the cells. We plan to eliminate these restrictions altogether by changing to a semi-implicit or implicit method of transferring the data between the Eulerian and Lagrangian grids, as is shown by Newren, Fogelson et al., in [26].

Finally, with large biofilm densities and viscosities, our multigrid method in its current formulation does

not converge as fast as expected. We plan to fix this by appropriately adapting our implementation of the geometric multigrid (by satisfying the Galerkin condition) or by changing to an algebraic multigrid approach.

9. Acknowledgements

References

[1] S. Aggarwal, E. H. Poppele, and R. M. Hozalski. Development and testing of a novel microcantilever technique for measuring the cohesive strength of intact biofilms. *Biotechnology and bioengineering*, 105(5):924–34, Apr. 2010.

[2] E. Alpkvist and I. Klapper. Description of Mechanical Response Including Detachment Using a Novel Particle Method of Biofilm/Flow Interaction. *Water Science and Technology*, 55(8-9):265–273, May 2007.

[3] N. Aravas and C. S. Laspidou. On the calculation of the elastic modulus of a biofilm streamer. *Biotechnology and bioengineering*, 101(1):196–200, Sept. 2008.

[4] K. Atkinson. *An Introduction to Numerical Analysis*. Wiley, New York, NY, 2nd edition, 1989.

[5] D. Balestrino, J.-M. Ghigo, N. Charbonnel, J. A. J. Haagensen, and C. Forestier. The characterization of functions involved in the establishment and maturation of Klebsiella pneumoniae in vitro biofilm reveals dual roles for surface exopolysaccharides. *Environmental microbiology*, 10(3):685–701, Mar. 2008.

[6] D. C. Bottino. Modeling Viscoelastic networks and cell deformation in the context of the immersed boundary method. *J. Computational Physics*, 147:86–113, 1998.

[7] W. L. Briggs, V. E. Henson, and S. F. McCormick. *A Multigrid Tutorial*. SIAM, Philadelphia, PA, 2000.

[8] D. L. Brown, R. Cortez, and M. L. Minion. Accurate Projection Methods for the Incompressible Navier-Stokes Equations. *Journal of Computational Physics*, 168(2):464–499, Apr. 2001.

[9] M. J. Chen, Z. Zhang, and T. R. Bott. Direct measurement of the adhesive strength of biofilms in pipes by micromanipulation. *Biotechnology Techniques*, 12(12):875–880, 1998.

[10] M. J. Chen, Z. Zhang, and T. R. Bott. Effects of operating conditions on the adhesive strength of *Pseudomonas fluorescens* biofilms in tubes. *Colloids and surfaces. B, Biointerfaces*, 43(2):61–71, June 2005.

[11] R. Cortez and M. Minion. The Blob Projection Method for Immersed Boundary Problems. *Journal of Computational Physics*, 161(2):428–453, July 2000.

[12] R. Dillon, L. Fauci, A. Fogelson, and D. Gaver III. Modeling Biofilm Processes Using the Immersed Boundary Method. *Journal of Computational Physics*, 129(1):57–73, Nov. 1996.

[13] J. H. Ferziger and M. Peric. *Computational Methods for Fluid Dynamics*. Springer, 3rd edition, 2002.

[14] W. X. Huang and H. J. Sung. An immersed boundary method for fluid-flexible structure interaction. *Computer Methods in Applied Mechanics and Engineering*, 198(33-36):2650–2661, 2009.

[15] J. C. Kissel, P. L. McCarty, and R. L. Street. Numerical Simulation of Mixed-Culture Biofilm. *Journal of Environmental Engineering*, 110(2):393–411, Apr. 1984.

[16] I. Klapper and J. Dockery. Mathematical Description of Microbial Biofilms. *SIAM Review*, 52(2):221, Oct. 2010.

[17] I. Klapper, C. J. Rupp, R. Cargo, B. Purvedorj, and P. Stoodley. Viscoelastic fluid description of bacterial biofilm material properties. *Biotechnology and bioengineering*, 80(3):289–96, Nov. 2002.

[18] J.-U. Kreft, G. Booth, and J. W. T. Wimpenny. BacSim, a simulator for individual-based modelling of bacterial colony growth. *Microbiology*, 144:3275–3287, 1998.

[19] J.-U. Kreft, C. Picioreanu, J. W. T. Wimpenny, and M. C. M. van Loosdrecht. Individual-based modelling of biofilms. *Microbiology*, 147(Pt 11):2897–2912, Nov. 2001.

[20] P. C. Y. Lau, J. R. Dutcher, T. J. Beveridge, and J. S. Lam. Absolute quantitation of bacterial biofilm adhesion and viscoelasticity by microbead force spectroscopy. *Biophysical journal*, 96(7):2935–48, Apr. 2009.

[21] R. J. LeVeque. *Finite Difference Methods for Ordinary and Partial Differential Equations: Steady-State and Time-Dependent Problems*. SIAM, Philadelphia, PA, 2007.

[22] Z. Li and K. Ito. *The Immersed Interface Method: Numerical Solutions of PDEs Involving Interfaces and Irregular Domains*, volume 33 of *Frontiers in Applied Mathematics*. SIAM, Philadelphia, PA, 2006.

[23] H. Luo, R. Mittal, X. Zheng, S. a. Bielamowicz, R. J. Walsh, and J. K. Hahn. An immersed-boundary method for flow-structure interaction in biological systems with application to phonation. *Journal of computational physics*, 227(22):9303–9332, Nov. 2008.

[24] S. Masuda, Y. Watanabe, and M. Ishiguro. Biofilm properties and simultaneous nitrification and denitrification in aerobic rotating biological contactors. *Water Science and Technology*, 23:1355–1363, 1991.

[25] Y. Mori and C. S. Peskin. Implicit second-order immersed boundary methods with boundary mass. *Computer Methods in Applied Mechanics and Engineering*, 197(25-28):2049–2067, Apr. 2008.

[26] E. P. Newren, A. L. Fogelson, R. D. Guy, and R. M. Kirby. Unconditionally stable discretizations of the immersed boundary equations. *Journal of Computational Physics*, 222(2):702–719, Mar. 2007.

[27] A. Ohashi and H. Harada. A novel concept for evaluation of biofilm adhesion strength by applying tensile force and shear force. *Water Science and Technology*, 34(5-6):201–211, 1996.

[28] L. Pavlovsky, J. G. Younger, and M. J. Solomon. In situ rheology of Staphylococcus epidermidis bacterial biofilms. *Soft Matter*, 9(1):122, 2013.

[29] C. S. Peskin. Numerical analysis of blood flow in the heart. *J. Computational Physics*, 81:372–405, 1977.

[30] C. S. Peskin. The immersed boundary method. *Acta Numerica*, 11:479–517, July 2002.

[31] C. Picioreanu, J.-U. Kreft, and M. C. M. van Loosdrecht. Particle-Based Multidimensional Multispecies Biofilm Model. *Applied and environmental microbiology*, 70(5):3024–3040, May 2004.

[32] C. Picioreanu, M. C. van Loosdrecht, and J. J. Heijnen. Two-dimensional model of biofilm detachment caused by internal stress from liquid flow. *Biotechnology and bioengineering*, 72(2):205–18, Jan. 2001.

[33] C. Picioreanu, M. C. M. van Loosdrecht, and J. J. Heijnen. Discrete-differential modelling of biofilm structure. *Water Science and Technology*, 39(7):115–122, 1999.

[34] C. Picioreanu, M. C. M. van Loosdrecht, and J. J. Heijnen. Effect of diffusive and convective substrate transport on biofilm structure formation: A two-dimensional modeling study. *Biotechnology and Bioengineering*, 69(5):504–515, Sept. 2000.

[35] B. E. Rittmann. Comparative performance of biofilm reactor types. *Biotechnology and bioengineering*, 24(6):1341–70, June 1982.

[36] B. E. Rittmann and P. L. McCarty. Evaluation of steady-state-biofilm kinetics. *Biotechnology and Bioengineering*, 22(11):2359–2373, Nov. 1980.

[37] K. S. Ro and J. B. Neethling. Biofilm density for biological fluidized beds. *Research Journal of the Water Pollution Control Federation*, 63(5):815–818, 1991.

[38] C. J. Rupp, C. A. Fux, and P. Stoodley. Viscoelasticity of Staphylococcus aureus biofilms in response to fluid shear allows resistance to detachment and facilitates rolling migration. *Applied and environmental microbiology*, 71(4):2175–8, Apr. 2005.

[39] R. Rusconi, S. Lecuyer, L. Guglielmini, and H. A. Stone. Laminar flow around corners triggers the formation of biofilm streamers. *Journal of the Royal Society, Interface / the Royal Society*, 7(50):1293–9, Sept. 2010.

[40] M. Spiga and G. Morino. A symmetric solution for velocity profile in laminar flow through rectangular ducts. *International Communications in Heat and Mass Transfer*, 21(4):469–475, July 1994.

[41] E. J. Stewart, A. Satorius, J. G. Younger, and M. J. Solomon. Impact of osmotic stress and sub-lethal antibiotic concentration on intercellular spacing and clustering in *Staphylococcus epidermidis* biofilms. *Submitted*.

[42] W. Strychalski and R. D. Guy. Viscoelastic Immersed Boundary Methods for Zero Reynolds Number Flow. *Communications in Computational Physics*, 12(2):462–478, 2012.

[43] K. G. Todar. Todar's Online Textbook of Bacteriology.

[44] Q. Wang and T. Zhang. Review of mathematical models for biofilms. *Communication in Solid State Physics*, 150(21-22):1009–1022, 2010.

[45] M. Zamir. *The Physics of Pulsatile Flow*. Biological Physics Series. Springer-Verlag, New York, NY, 2000.

[46] T. Zhang, N. G. Cogan, and Q. Wang. Phase Field Models for Biofilms. I. Theory and One-Dimensional Simulations. *SIAM Journal on Applied Mathematics*, 69(3):641, 2008.

[47] T. Zhang, N. G. Cogan, and Q. Wang. Phase-field models for biofilms II. 2-D numerical simulations of biofilm-flow interaction. *Commun. Comput. Phys*, 4(1):72–101, 2008.

[48] L. Zhu and C. S. Peskin. Simulation of a Flapping Flexible Filament in a Flowing Soap Film by the Immersed Boundary Method. *Journal of Computational Physics*, 179(2):452–468, July 2002.

[49] J. Zhuo and R. Dillon. Using the immersed boundary method to model complex fluids-structure interaction in sperm motility. *Discrete and Continuous Dynamical Systems - Series B*, 15(2):343–355, Dec. 2011.

Appendix A.

In this appendix we provide a list of variables and parameters used in this paper.

b Dashpot Damping Coefficient

d_0 Average Spring Rest Length

δ Dirac Delta Function

δ_h Discretized Dirac Delta Function from Peskin

$\tilde{\delta}$ Our Modified Discretized Dirac Delta Function

D Spatial dimension, $D = 2$ for 2D simulations and $D = 3$ for 3D simulations

$\mathbf{e}_i$ Unit Vector in the ith direction

η Total Number of Lagrangian Points

$\mathbf{f}$ Eulerian Force Density

$\mathbf{F}$ Lagrangian Force

F_{max} Maximum Lagrangian Force

h Spatial Discretization of finest grid

K Hookean Spring Coefficient

μ Dynamic Fluid Viscosity

μ_{max} Maximum Biofilm Viscosity

p Pressure

$\mathbf{q} = (q, r, s)$ Lagrangian Coordinates

ρ Density

ρ_0 Uniform Fluid Density

ρ_b Additional Density in Biofilm

s Lagrangian Node Marker

t Time

T Tension in Spring

$\mathbf{u}$ Eulerian Velocity

$\tilde{\mathbf{u}}$ Intermediate Velocity

$\mathbf{U}$ Lagrangian Velocity

$\mathbf{x} = (x_1, x_2, x_3)$ Cartesian Coordinates

Appendix B. Scaling Parameters

Scaling Parameters			
Description	Scaling parameter	Primary dimensions	Specific values chosen for simulations
Characteristic Length	L	$\{L\}$	$50\,microns$
Characteristic Speed	u_0	$\{L/t\}$	$10^{-3}\,m/s$
Characteristic Frequency	T	$\{t\}$	$1\,s$
Reference Pressure Difference	$p_0 - p_{L_{tube}}$	$\{mL^{-1}t^{-2}\}$	$.8144\,Pa$
Characteristic Density	ρ_0	$\{mL^{-3}\}$	$998\,kg/m^3$
Characteristic Viscosity	μ	$\{mL^{-1}t^{-1}\}$	$10^{-3}\,kg/ms$
Characteristic Force Density	f_0	$\{F/L^3\}$	$varies$

Table B.10: Shows the scaling parameters and their descriptions.